



HAL
open science

Cross-Scale Processes of Magnetic Reconnection

K. -J. Hwang, R. Nakamura, J. P. Eastwood, S. A. Fuselier, H. Hasegawa, T. Nakamura, B. Lavraud, K. Dokgo, D. L. Turner, R. E. Ergun, et al.

► **To cite this version:**

K. -J. Hwang, R. Nakamura, J. P. Eastwood, S. A. Fuselier, H. Hasegawa, et al.. Cross-Scale Processes of Magnetic Reconnection. *Space Science Reviews*, 2023, 219, 10.1007/s11214-023-01010-9. insu-04473113

HAL Id: insu-04473113

<https://insu.hal.science/insu-04473113v1>

Submitted on 23 Feb 2024

HAL is a multi-disciplinary open access archive for the deposit and dissemination of scientific research documents, whether they are published or not. The documents may come from teaching and research institutions in France or abroad, or from public or private research centers.

L'archive ouverte pluridisciplinaire **HAL**, est destinée au dépôt et à la diffusion de documents scientifiques de niveau recherche, publiés ou non, émanant des établissements d'enseignement et de recherche français ou étrangers, des laboratoires publics ou privés.



Distributed under a Creative Commons Attribution 4.0 International License



Cross-Scale Processes of Magnetic Reconnection

K.-J. Hwang¹ · R. Nakamura² · J.P. Eastwood³ · S.A. Fuselier¹ · H. Hasegawa⁴ · T. Nakamura^{5,6} · B. Lavraud⁷ · K. Dokgo¹ · D.L. Turner⁸ · R.E. Ergun⁹ · P.H. Reiff¹⁰

Received: 13 July 2023 / Accepted: 30 September 2023 / Published online: 30 October 2023
© The Author(s) 2023

Abstract

Various physical processes in association with magnetic reconnection occur over multiple scales from the microscopic to macroscopic scale lengths. This paper reviews multi-scale and cross-scale aspects of magnetic reconnection revealed in the near-Earth space beyond the general global-scale features and magnetospheric circulation organized by the Dungey Cycle. Significant and novel advancements recently reported, in particular, since the launch of the Magnetospheric Multi-scale mission (MMS), are highlighted being categorized into different locations with different magnetic topologies. These potentially paradigm-shifting findings include shock and foreshock transient driven reconnection, magnetosheath turbulent reconnection, flow shear driven reconnection, multiple X-line structures generated in the dayside/flankside/nightside magnetospheric current sheets, development and evolution of reconnection-driven structures such as flux transfer events, flux ropes, and dipolarization fronts, and their interactions with ambient plasmas. The paper emphasizes key aspects of kinetic processes leading to multi-scale structures and bringing large-scale impacts of magnetic reconnection as discovered in the geospace environment. These key features can be relevant and applicable to understanding other heliospheric and astrophysical systems.

Keywords Magnetic reconnection · Bow shock · Foreshock transient · Magnetosheath · Turbulent reconnection · Flow shear · Flux rope · Flux transfer event · Dipolarization front · Magnetospheric multi-scale mission · Electron-only reconnection · Flow vortex · Electron vortex · Kelvin-Helmholtz instability · Kelvin-Helmholtz wave · Kelvin-Helmholtz vortex · Mid-latitude reconnection · Current sheet flapping · Substorm · Solar wind transport

1 Introduction

This paper addresses recent advancements to understand the cross-scale processes that unify the kinetic physics operating during magnetic reconnection (Genestreti et al., Liu et al., Norgren et al., this collection) and global magnetospheric context of reconnection (Fuselier et al., this collection), as well as reconnection in other regimes encompassing solar and planetary physics (Gershman et al., Drake et al., this collection). Magnetic reconnection is initiated in the electron diffusion region (EDR; microscales) where electrons are demagnetized and electron physics dominates, and then entails dynamics in the ion diffusion region (IDR; mesoscales) where ions are demagnetized and Hall physics due to ion-electron decoupling

Extended author information available on the last page of the article

becomes important. The region where electron jets from the EDR brake and electrons become re-magnetized is called the outer EDR. Across the diffusion region, the energy stored in the magnetic field is converted into particle energy. The separatrix is the narrow line (in 2-D) or surface (in 3-D) that separates inflowing and outflowing plasmas before and after undergoing the reconnection process. Reconnection ultimately propagates its effect to the macroscopic or global (scale sizes of Earth radii, R_E) region where magnetohydro-dynamics (MHD) governs. Even though these sub-structures show distinct physical features, they adjoin each other and interact by exchanging/transporting particles, momentum, and energy. Therefore, the reconnection process is intrinsically multi-scale and cross-scale with different physics predominantly identified at each boundary layer of different scales.

The near-Earth space provides the most accessible laboratory for the multi-scale physics at work during reconnection that can be applied to various heliospheric systems as well as laboratory plasma experiments. In particular, a key advantage of geospace observations is that all relevant (from microscopic to macroscopic) scales are separated to the extents measurable by in situ. E.g., the EDR ranges on the order of electron gyroradius (ρ_e) or electron inertial length (d_e), which is ~ 5 km in Earth's dayside magnetopause and ~ 30 km in the nightside magnetotail. On the other hand, e.g., ρ_e in solar corona is of the order of 1 m, much smaller than observable scales. Therefore, comprehensive understanding of the terrestrial plasma system will fill the gaps between theoretical/analytic predictions and in-situ observations of micro-to-macro-scale processes that underly reconnection occurring throughout the heliosphere and the universe.

Two of the most fundamental and long-standing science questions in near-Earth plasma physics are how plasmas are transported and how particles are energized (Oka et al., this collection). The large-scale magnetospheric convection regarding the former has been described as the Dungey Cycle, which is powered by dayside and nightside reconnection (Fuselier et al., this collection). This global and general picture, however, leaves important missing links in cross-scale aspects of reconnection in the terrestrial environment. Frequently-occurring and recently-highlighted ingredients attributed to the multi-scale nature reconnection include, but are not limited to: reconnection upstream of, at, or downstream of the bow shock; the coupled shock-reconnection-turbulence process whose effects convect to the dayside magnetopause and affect dayside reconnection; formation, extent, and orientation of an X-line depending on the background magnetic topologies; development and evolution of multiple X-lines, resultant multi-scale structures, and their interactions with ambient plasmas; and velocity shear effects on reconnection and flow shear-driven reconnection.

This paper focuses on bridging these gaps in cross-scale aspects of magnetic reconnection via understanding the reconnection onset and the structure, evolution, and consequences of reconnection that can be organized in terms of the location in the geospace. For example, reconnection at/around the bow shock is often characterized by turbulent micro-to-meso-scale current sheets. The dayside magnetopause current sheet is typically asymmetric with a significant guide field, whereas the nightside magnetotail current sheet is generally symmetric along the current sheet normal direction with no or little guide field. The tail current sheet is, however, asymmetric along the nominal magnetic field direction, i.e., the x direction in geocentric solar magnetospheric coordinates (GSM). The current sheets formed at higher latitudes than the equatorial dayside magnetopause or developed along the flankside magnetopause are subject to large velocity shear. Although the tearing instability is suppressed by the velocity shear, the flow shear-driven instability can compress an initially thick current sheet, triggering reconnection. These different reconnection geometries and magnetic topologies lead to different extent and orientation of the X-line, which subsequently drives

various channels for the evolution and consequence of reconnection including 3-D and/or multi-scale structures. Thus, we structure this paper as follows:

1. Introduction

2. Reconnection in the shock region and magnetosheath

2.1 Introduction

2.2 Reconnection in the shock transition region

2.3 Reconnection in the foreshock

2.4 Interaction of discrete current sheets with the bow shock and associated reconnection onset

2.5 Influence of shock dynamics and reconnection on the downstream magnetosheath

3. Reconnection in the dayside magnetopause

3.1 Introduction

3.2 Multi-scale aspects of dayside reconnection processes

3.3 Extent of reconnection X-lines and 3-D complexities

3.4 Flux ropes and Flux transfer events (FTEs)

4. Reconnection in the flankside magnetopause

4.1 Introduction

4.2 In-plane 2-D reconnection in the presence of a velocity shear

4.3 Mid-latitude reconnection associated 3-D magnetic topologies

4.4 Plasma mixing, transport, and turbulence

5. Reconnection in nightside magnetotail

5.1 Introduction

5.2 Onset conditions for local/global current sheet thinning

5.3 Multi-scale aspects of the nightside reconnection region

5.4 Transient structures in the exhaust region

6. Key aspects with relevance and applications to other plasma systems

The importance of multi-scale perspectives of reconnection has been indicated by recent multi-point in-situ measurements and integration with state-of-the-art numerical simulations. Each section introduces the topic that has drawn wide attention among the magnetospheric community, what is currently known, and what remains elusive about the topic. We highlight what advancements have been achieved by the high time-resolution dataset from the four Magnetospheric Multi-scale (MMS) satellites of inter-spacecraft spacing down to electron scales. We address how these findings can be a key to connect the missing links in the multi-scale reconnection process that is applicable to other heliospheric or astrophysical systems.

2 Reconnection in the Shock Region and Magnetosheath

2.1 Introduction

Shocks, reconnection, and turbulence are often held up as three processes that are fundamental to understanding plasmas, particularly in the space environment. This is, in part, because they all control the transport and repartition of energy. This issue is generally of importance

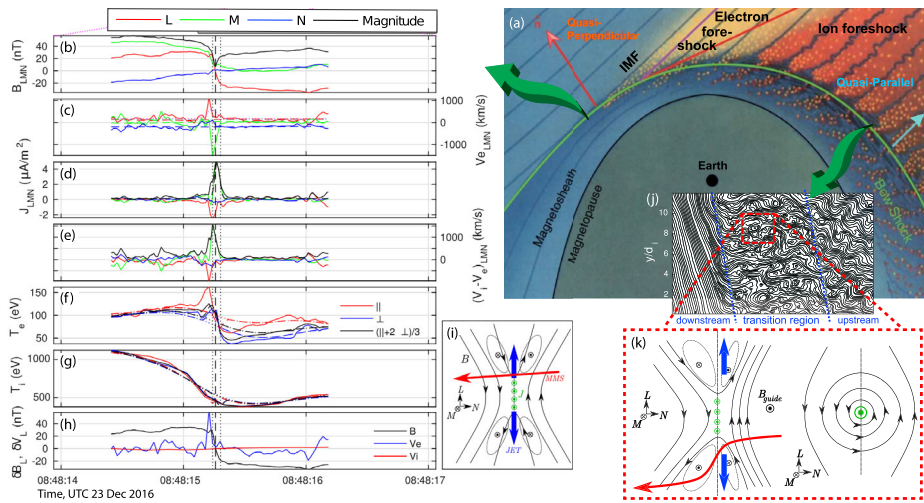


Fig. 1 (a) Schematic of Earth's shock, foreshock, and magnetosheath (adopted from Balogh and Treumann 2013). (b–i) Adopted from Gingell et al. (2020) showing a small-scale reconnection event in the transition region of the quasi-perpendicular shock observed by MMS. The reconnection current carried mostly by electrons (c–e) and electron outflow jet (h; blue profile) indicate that MMS traversed the current sheet undergoing reconnection along the trajectory shown as a red arrow in panel (i). (j, k) Illustration of the quasi-parallel shock structure and the expanded view of the reconnecting current sheet and the magnetic null observed in the turbulent transition region (adopted from Gingell et al. 2019)

in astrophysics where collisionless shocks are believed to be important for creating energetic particles in a variety of circumstances (e.g., Bohdan et al. 2020; Matsumoto et al. 2015).

Prior to the launch of MMS, it was increasingly understood that these three processes may well co-exist in a more tightly-coupled sense (e.g., Karimabadi et al. 2014). The turbulence properties were found to be qualitatively different downstream from the quasi-parallel shock ($\theta_{Bn} < 45^\circ$, where θ_{Bn} is the angle between the shock normal and the interplanetary magnetic field, IMF; Fig. 1a) and quasi-perpendicular shock ($\theta_{Bn} > 45^\circ$). Field-aligned populations backstreaming from the quasi-parallel shock give rise to the formation of the extended foreshock, where the counterstreaming component interacts with the pristine solar wind plasma generating waves, which penetrate the shock, leading to more turbulent magnetosheath (Fig. 1a). Important evidence from Cluster demonstrated the existence of thin ion-scale current sheets in the turbulent magnetosheath exhibiting reconnection signatures in the electric and magnetic field (Retinò et al. 2007; Sundkvist et al. 2007). These studies highlighted the importance of the shock itself as an interplay between turbulence and reconnection.

Notable progress has since stemmed from the analysis of MMS observations of the shock, foreshock, and magnetosheath. A number of studies show that reconnection can operate in all of these regions on a variety of scales, providing a pathway to new understanding of how shocks, turbulence, and reconnection co-exist as well as revealing new questions.

Here we review recent important studies concerning reconnection in the coupled foreshock, bow shock, and magnetosheath system as well as the interplay between turbulence and reconnection. Instead of a comprehensive review of MMS-based magnetosheath reconnection studies detailed in Stawarz et al. (this collection), we focus on multi-scale aspects of the bow shock and its vicinity together with their effect and impact on the dayside magnetopause dynamics to be discussed in Sect. 3.

2.2 Reconnection in the Shock Transition Region

The shock transition region is the front side (ramp) of the shock where the flow speed decreases gradually from the upstream to the shocked downstream region. MMS has provided evidence of magnetic reconnection in the shock transition region for both quasi-perpendicular and quasi-parallel shock configurations. An example for the former is illustrated in the Fig. 1(b-i) event on 23 Dec 2016, where $\theta_{Bn} \sim 85^\circ$. A coordinate system used in Fig. 1 represents the maximum (L), intermediate (M) and minimum (N) variance directions of the magnetic field over the current sheet crossing. The magnetic field reversal (Fig. 1b, h) is coincident with the electron jet and temperature peak (Fig. 1c, e, h), indicative of electron-engaged reconnection. Another quasi-perpendicular-shock case study from 9 Nov 2016 (Wang et al. 2019), where $\theta_{Bn} \sim 60^\circ$, identified both the diffusion region and a separate reconnection exhaust. In the diffusion region, Hall electric and magnetic fields were observed as well as enhanced local energy conversion. In the exhaust region observed a few seconds earlier, accelerated ion flow was observed together with evidence of multi-beam mixed populations in a current sheet of ~ 4 ion inertial lengths (d_i) half-thickness.

At the quasi-parallel shock with $\theta_{Bn} = 21^\circ$ (Gingell et al. 2019), many small-scale current sheets were observed in a transition region of ~ 2 minute duration crossing on 26 Jan 2017 as shown in the sketch in Fig. 1j. Reconnection was identified at one such current sheet (Fig. 1k). An unexpected feature was that although the reconnecting current sheet was apparently ion scale in thickness ($\sim 3 d_i$), only an electron jet was observed. Whilst similar to the MMS observations of electron-only reconnection in the magnetosheath (Phan et al. 2018), it was proposed that the thicker current sheet could be younger than an ion-gyroperiod and therefore in the early stage of its development, consistent with the proximity of the observation to the shock ramp.

Further analysis of both these events, and another event reported in Gingell et al. (2019) used the First Order Taylor Expansion (FOTE) (Fu et al. 2015) to identify the existence of magnetic nulls in the vicinity of MMS (Fig. 1k) when MMS was close to the X-line rather than in the exhaust (Chen et al. 2019). This reconstruction also enabled the reconnection rate to be estimated, finding that it is comparable to observations both in the magnetotail and at the magnetopause.

A follow-up study examining ~ 900 MMS events of the bow shock observations made in burst mode (Gingell et al. 2020) found that actively reconnecting current sheets were a feature of $\sim 40\%$ of shock crossings and observed in both quasi-parallel and quasi-perpendicular geometries. Given that reconnecting current sheets were encountered for all observed Mach numbers (in addition to θ_{Bn}), it is suggested that reconnection within the shock transition region is a universal process. However, quasi-parallel and high Alfvén Mach number cases exhibited reconnecting current sheets more frequently. In general, the reconnection events were found to typically show only weak ion heating and ion jets with preferential electron coupling. Moreover, the current sheets were reported to be thicker than those observed in the turbulent magnetosheath, and with slower electron jets.

Simulations, as illustrated in Fig. 2, support interpreting and understanding novel MMS observations of reconnection in the shock transition region. The 2-D PIC (particle-in-cell) simulations of a quasi-parallel shock ($\theta_{Bn} = 25^\circ$) showed that reconnecting current sheets form both in the transition region of the shock and downstream (Bessho et al. 2019), with good agreement to observations made by MMS (Bessho et al. 2022).

Similarly, at quasi-perpendicular shocks it has been shown that cyclical reformation of the shock front leads to the formation of small current sheets where electron-only reconnection may occur (Lu et al. 2021). In general, for high Mach number shocks the shock

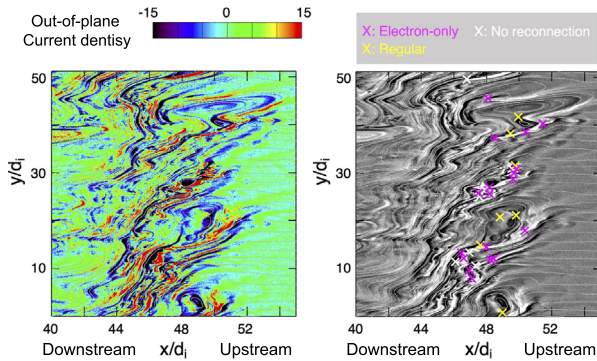


Fig. 2 Abundant current sheets formed in the shock transition and downstream regions of a quasi-parallel shock (adopted from Bessho et al. 2022). In the simulation domain plasmas flow from right (upstream) to left (downstream). Left panel shows the out-of-plane current density. In the right panel, electron-only and regular (both ion and electron-involving) reconnection sites are marked in magenta and yellow, respectively. Regardless of electron-only or regular reconnection, the reconnection rate ranges between 0.1 and 0.2 (Bessho et al. 2019)

transition tend to become more turbulent with more reconnection sites, exhibiting electron-only reconnection on ion-scale current structures (Bessho et al. 2020). This study further revealed that non-reconnecting current sheets with the magnetic field reversal are also sites for the field-to-particle energy conversion, indicating that this feature is not unique to reconnection events. The energy conversion rate ($\mathbf{J} \cdot \mathbf{E}'$, where \mathbf{J} is the electric current and \mathbf{E}' is the electric field in the electron frame) in non-reconnecting current sheets is, however, smaller than that in reconnecting current sheets.

These data-model analyses provide important context for how shocks, turbulence and reconnection co-exist. In particular, the reconnection rate in the electron-only reconnection current sheets was obtained to be between 0.1 and 0.2, similar to the regular reconnection rate around 0.1 (Bessho et al. 2019). This further poses a new question, whether or not electron-only reconnection is the evolutionary stage before reaching the ion reconnection.

2.3 Reconnection in the Foreshock

The foreshock is defined as the region upstream of the bow shock that is magnetically connected to the shock and contains particles backstreaming from the shock. The combination of backstreaming particles and the inflowing solar wind makes velocity distribution functions subject to a variety of instabilities on a range of spatial and temporal scales, leading to wave generation and particle acceleration/thermalization. The continuously varying solar wind means that the foreshock is not a purely static region but can host a number of transient structures. In particular, the interaction of discontinuities in the solar wind magnetic field with the bow shock can cause changes in particle reflection and localized transient regions of enhanced thermal pressure that may also play a role in particle acceleration processes. These transients are often identified as hot flow anomalies and foreshock bubbles (Archer et al. 2015; Schwartz 1995). Data from MMS has provided new insight and understanding about the role played by reconnection in foreshock dynamics.

In a survey of foreshock transients observed by MMS (Liu et al. 2020), evidence of reconnection was found in five examples of foreshock transients from an examination of 130 events over 2 years of MMS observations. Both anti-parallel and strong guide field reconnection events were reported as shown in Fig. 3. In both cases electron-only reconnection in

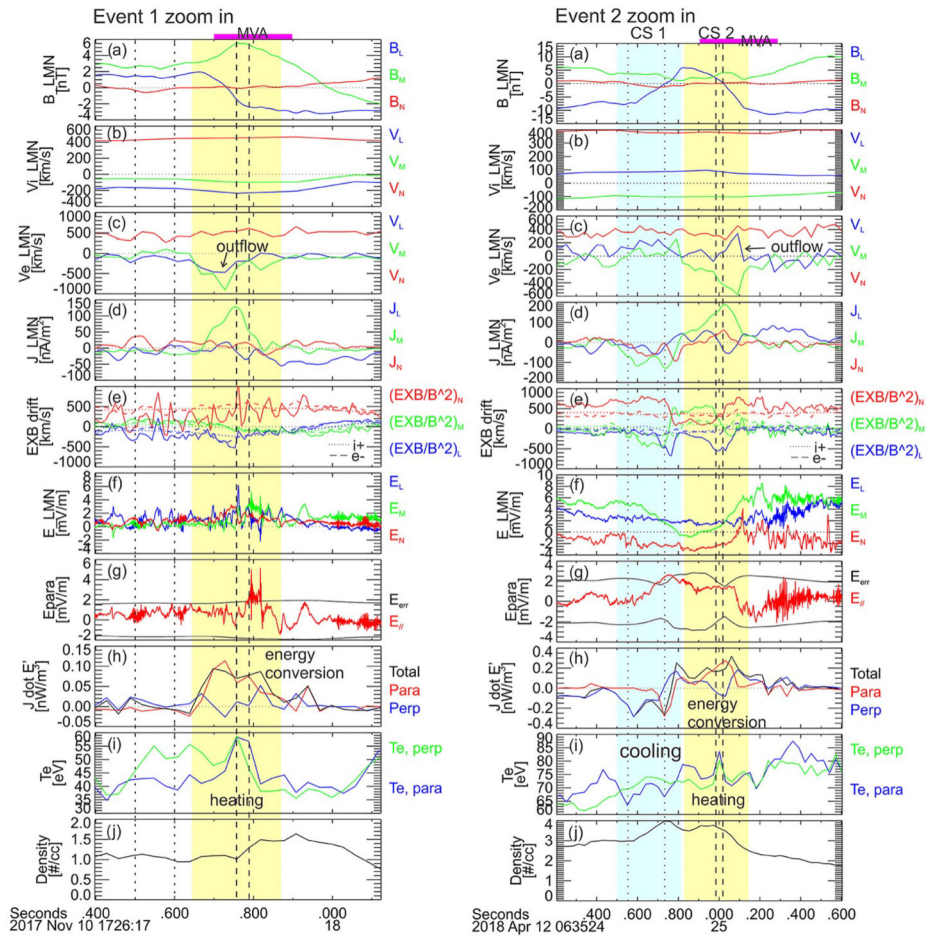


Fig. 3 Adopted from Liu et al. (2020). Two MMS events compare reconnection with a strong guide field (left) and no guide field (right) observed in the turbulent region of a foreshock transient. Both events show electron-only outflows (panel c), indicating electron-only reconnection in a thin ($\sim 1 d_i$) current sheet. The guide-field reconnection event shows more dominant heating and energy conversion along the parallel direction within the current sheet (bounded by vertical dashed lines)

a thin ($\sim 1 d_i$) current sheet was identified in the turbulent interior of a foreshock transient. These events (particularly the guide field event) were in many ways similar to observations of electron-only reconnection in the turbulent magnetosheath (Phan et al. 2018). This demonstrates a new role for turbulent reconnection in potentially contributing to the energization of particles in the foreshock, which is relevant for understanding the production of seed populations that undergo subsequent energization during the shock crossing and further downstream the shock.

Magnetic reconnection can be responsible for the formation of flux ropes. Within the foreshock MMS has observed a flux rope inside a hot flow anomaly (Bai et al. 2020). This complements previous (prior to MMS) observations of a flux rope confined inside a hot flow anomaly in the magnetosheath (Hasegawa et al. 2012). Bai et al. (2020) reported a small flux rope (size of 6–8 d_i) encountered at the trailing edge of the hot flow anomaly. A flux

rope was not observed by the Wind spacecraft in the upstream solar wind, thus the flux rope was likely to be locally generated, potentially triggered by the interaction of the underlying discontinuity and the bow shock.

Jiang et al. (2021) used MMS observations in conjunction with the first-order Taylor expansion (FOTE) method to infer the existence of reconnecting current sheets in the foreshock more generally. In two separate examples from the dawn- and dusk-side foreshock, but both upstream of the quasi-parallel shock, thin current sheets were observed to exhibit electron-only reconnection signatures, consistent with magnetic geometry derived from the FOTE analysis.

2.4 Interaction of Discrete Current Sheets with the Bow Shock and Reconnection Onset

It is well established that reconnection occurs in large scale current sheets in the solar wind (e.g., Gosling 2012). These current sheets are convected in the solar wind flow through the bow shock, leading to large-scale reconnection observed in the magnetosheath (e.g., Øieroset et al. 2017). Although the MMS instrumentation is not optimized to observe solar wind reconnection per se, it is capable of resolving such current sheets in the magnetosheath. MMS has provided new, detailed information about large-scale reconnection current sheets in the magnetosheath that likely originated in the solar wind, revealing the following features: evidence of reconnection at $\sim 100 d_i$ downstream from the X-line; asymmetric Hall electric and magnetic fields and inhomogeneous (predominantly parallel) ion and electron heating across the exhaust associated with the guide field; a density cavity confined near one edge of the exhaust where electron cooling and enhanced ion heating occur due to the parallel electric field (Eastwood et al. 2018).

When interacting with the bow shock, or near to the magnetopause in the magnetosheath, a non-reconnecting current sheet can be compressed (Kropotina et al. 2021), which can lead to the onset of reconnection in the magnetosheath (Maynard et al. 2007; Phan et al. 2007). Pre-MMS observations suggested that the interaction of a current sheet with the shock can interrupt reconnection, with it being triggered again by compression at the magnetopause (Phan et al. 2011). During a quasi-perpendicular shock crossing on 20 Dec 2015, a solar wind discontinuity was fortuitously observed by MMS embedded just behind the shock front (Hamrin et al. 2019). Although not in burst mode, MMS provided evidence for Hall fields and particle energization indicating ongoing reconnection. By comparing with multiple other satellites in the solar wind, foreshock, and magnetosheath it was concluded that the observed reconnection was triggered by the compression of the discontinuity at the shock.

Global 3-D hybrid simulations of the dayside shock region have shed further light on this process. A simulation of the interaction of a rotational discontinuity with 180° magnetic shear with the quasi-perpendicular shock suggests that reconnection can be triggered by the shock compression leading to the formation of reconnection jets and flux ropes, initially on ion scales (Guo et al. 2021a). Other simulations focusing on the interaction of rotational discontinuities with the quasi-parallel shock reveal more complex behavior. In particular, the discontinuity can be affected by the enhanced fluctuations in the foreshock, causing more complex structure and local current sheet thinning and reconnection (Guo et al. 2021b).

2.5 Influence of Shock Dynamics and Reconnection on the Downstream Magnetosheath

On the question of how the shock influences the magnetosheath, data from MMS has provided apparently conflicting conclusions. Yordanova et al. (2020) concluded that behind the

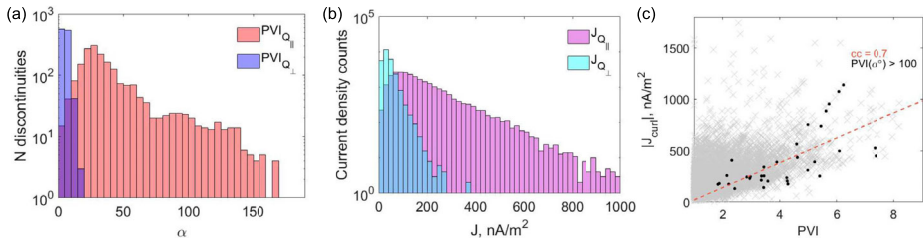


Fig. 4 Adopted from Yordanova et al. (2020). Statistics of the occurrence of discontinuities as a function of the magnetic shear (α) measured from pairs of MMS spacecraft separated by 0.25 s (a). In the quasi-perpendicular magnetosheath, the PVI, a measure of structural coherency, is concentrated mostly at $\alpha < 10^{\circ}$. The quasi-parallel case shows the distribution over the entire range of α with heavy tail for $\alpha > 90^{\circ}$. The heavy tail is associated with the presence of currents as confirmed by the histogram of the current density (b). The current density and the PVI (c) for the quasi-parallel magnetosheath shows a good correlation (c) in particular for black dots ($\alpha > 100^{\circ}$), potentially corresponding to reconnecting current sheets

quasi-parallel shock the magnetosheath exhibits stronger current sheets and discontinuities (Fig. 4) whereas Gingell et al. (2021) examined the prevalence of thin current sheets in the magnetosheath, finding no strong dependence on the local plasma beta or the shock θ_{Bn} and Alfvén Mach number. The two analyses used different approaches. The former employed the Partial Variance of Increments (PVI) approach for detection of coherent structures such as current sheets (Greco et al. 2018) and the latter directly searched for discrete 1-D current sheet structures. Gingell et al. (2021) suggested that the unexpectedly low prevalence in the quasi-parallel magnetosheath could be due to the difficulty of designing automated routines to identify current sheets in a more generally disturbed plasma. In simulations, global 3-D hybrid modelling has shown that foreshock waves can pass through the shock, where they are compressed and can undergo reconnection (Lu et al. 2020). While this type of simulation cannot capture electron-only reconnection, it provides further insight into the differences between the magnetosheath downstream of different bow shock magnetic geometries, which remains an active area of research.

Of particular interest is the role that thin current sheets embedded in the turbulent downstream flow of the shock may play in energization, and therefore the overall energy conversion process that the solar wind experiences as it flows around the magnetosphere. In a case study of a quasi-parallel shock which benefited from a very long acquisition of MMS burst mode data on 21 Dec 2017, thin current sheets were found to occupy 3% of the downstream magnetosheath volume with many of them showing evidence of reconnection (Schwartz et al. 2021). These current sheets were estimated to process 5–11% of the upstream energy flux incident at the bow shock. This indicates that these thin current sheets initiated at the bow shock continue to influence energy processing throughout the downstream magnetosheath to the arrival at the dayside magnetopause. The detailed pathways and impacts of these fluctuations driven by reconnection, shock, and turbulence toward the magnetopause and beyond require further investigation.

3 Reconnection in the Dayside Magnetopause

3.1 Introduction

The dayside magnetopause reconnection current sheet is characterized by local asymmetries that arise from the density gradient across the magnetopause, a velocity shear in the

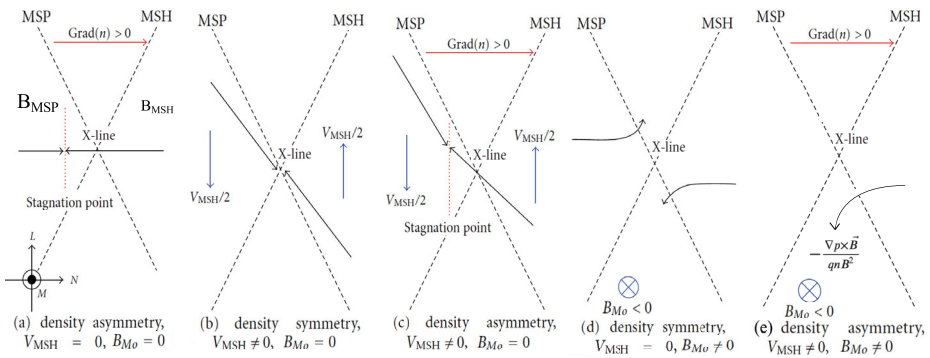


Fig. 5 Three elements driving asymmetries of the dayside magnetopause current sheet are the density gradient (panels a, c, and e), a velocity shear (b, c), and a guide field (d, e). In each panel, the magnetospheric (magnetosheath) region is on the left (right). Effects of each of these and combined effects are illustrated (adopted from Tanaka et al. 2010). The boundary coordinate system represents the maximum (L), intermediate (M) and minimum (N) variance directions of the magnetic field over the current sheet crossing

reconnection plane across the current sheet, and the presence of a guide field (Fig. 5). The density asymmetry leads to a shift in the flow stagnant point toward the low-density magnetospheric side from the X-line due to the high-density magnetosheath plasmas that carry momentum (Fig. 5a). In the presence of a velocity shear (Fig. 5b), which is expected at the high-latitude dayside magnetopause away from the subsolar region, the inflow is slanted from the normal direction. When the two are combined (Fig. 5c), the X-line site is occupied by magnetosheath plasmas, resulting in an L-directional X-line drift. A guide field creates a similar slanted inflow due to the Lorentz force, which occurs near the center of the current sheet (Fig. 5d).

When the density gradient is combined with a guide field (Fig. 5e), the diamagnetic effect controls the drift of an X-line. If the diamagnetic drift is larger than the outflow speed, reconnection ceases to operate (Swisdak et al. 2010, 2003). The presence of a velocity shear (Fig. 5b and 5c) has, in general, a similar effect on the reconnection rate as diamagnetic suppression (Fig. 5e) since the slanted inflow decreases the efficiency of the reconnected field line to drive the outflow (La Belle-Hamer et al. 1995; Cassak and Otto 2011; Doss et al. 2015).

These asymmetries across the dayside magnetopause give rise to significant variations in the multi-scale boundaries of the reconnecting current layer. The density asymmetry (Fig. 5a) leads to the deviation from the quadrupolar Hall fields: strong Hall E_N along the magnetospheric separatrix region; more bipolar than quadrupolar Hall B_M . The effect of a guide field (Fig. 5d) further introduces the quadrupolar density variation and asymmetric quadrupolar Hall fields. (See more details in Genestreti et al., this collection.) The effect of a velocity shear (Fig. 5b), which is most ubiquitous in the flankside magnetopause, is discussed in Sect. 4.1.

The following subsections focus on the multi-scale characteristics of dayside reconnection (Sect. 3.2), the extent and orientation of the X-line over the surface of the dayside magnetopause (Sect. 3.3), and evolution and consequences of dayside reconnection such as flux ropes and flux transfer events (Sect. 3.4).

3.2 Multi-Scale Aspects of Dayside Reconnection Processes

Typical scale lengths of the terrestrial dayside magnetopause current layers are on the order of d_e (the electron inertial length; ~ 5 km) for EDR, d_i (the ion inertial length; ~ 200 km) for IDR, and thousands of km to tens of R_E for, e.g., the length of an X-line. The first observation of the EDR at the dayside magnetopause was made by MMS (Burch et al. 2016). The high time-resolution MMS data revealed typical features of the EDR, including electron agyrotropy, i.e., electron crescent distribution in the plane perpendicular to the magnetic field, electron jet reversal, and positive Ohmic energy exchange, as predicted from PIC simulations (Hesse et al. 2014).

Using these common features of the EDR, Webster et al. (2018) reported 32 MMS events of the dayside reconnection EDR. Small separation between the four MMS spacecraft down to electron scales enabled evaluating relative contributions of each term in the generalized Ohm's law. Webster et al. (2018) showed general agreement between the reconnection electric field and the gradient of the electron pressure tensor, while presenting a wide range of electron distribution and energy exchange patterns around the EDR. Torbert et al. (2016) found that the electron inertial term in the generalized Ohm's law is not negligible in the EDR. The EDR was found to be unaffected by turbulence, as seen in a magnetotail reconnection event (Ergun et al. 2022) where the electron physics in a turbulent EDR does not differ from a laminar EDR (Sect. 5.3).

Hwang et al. (2017) reported observations where MMS passed through the edge of the elongated EDR (i.e., the outer EDR) in the dayside reconnection current sheet. Characteristics of the outer EDR included the parallel electron crescent distribution and the out-of-plane electric field exhibiting an opposite polarity to the reconnection electric field. The former (Fig. 6b) is explained by cyclotron turning of the accelerated electrons by the reconnected magnetic field in the outer EDR (Chen et al. 2016). The latter is caused by the electron outflow jet outrunning the moving magnetic field, as evidenced by the observed energy conversion from bulk kinetic energy to field and thermal energy (Zenitani et al. 2011; Chen et al. 2016; Fig. 6a). This indicates the outer EDR as an ingredient in the energy partition during reconnection.

The role of the outer EDR in the cross-scale coupling of reconnection was further investigated by Genestreti et al. (2020). They used the MMS observation of the interface between the EDR and the IDR to assess how electron-scale dynamics affect the ion-scale reconnection rate (Fig. 6c-d). The Hall electron flow in the high-density magnetosheath side leads to the formation of intense pileup of reconnected magnetic flux, consistent with energy conversion from electron kinetic energy to field energy. Thus, electron dynamics affects the opening angle, which is closely related to the reconnection rate.

At the nearby EDR, electron-scale magnetic field fluctuations were observed (Hoilijoki et al. 2021). The higher (lower) reconnection rate can make the opening angle larger (smaller) by increasing (decreasing) the magnetic field pileup. Thus, time variation of the reconnection rate can result in the magnetic field fluctuations. Another generation mechanism for electron-scale magnetic field fluctuations is electron vorticity due to electron Kelvin-Helmholtz instability (Fermo et al. 2012).

The separatrix is an active region where reconnection inflows and outflows are mixed. In the separatrix of dayside reconnection, spiky parallel electric field structures are observed, including double layers and electrostatic solitary waves (Genestreti et al. 2020; Holmes et al. 2019; Hwang et al. 2017). The two-stream instability between inflow and outflow electron plasma, the bump-on-tail instability due to high-speed tail, and the Buneman instability caused by different drifts of ions and electrons can all be important in this region of mixing

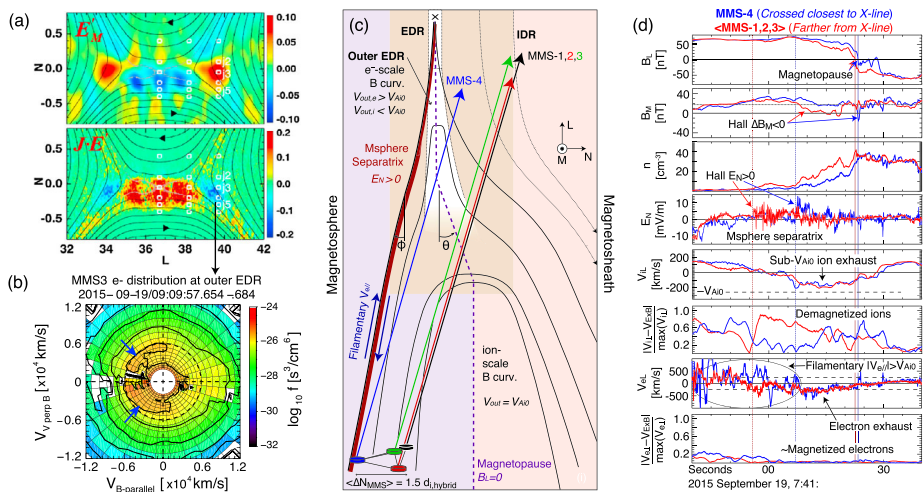


Fig. 6 (a–b) Adapted from Chen et al. (2016) and Hwang et al. (2017) showing the out-of-plane electric field of an opposite polarity to the reconnection electric field, negative Ohmic energy exchange, and parallel electron crescent in the outer EDR. (c–d) Adopted from Genestreti et al. (2020). MMS1–3 passed the IDR, while MMS4 went closer to the EDR through IDR and outer EDR. MMS observed substructures of the IDR including the Hall fields and super-Alfvénic electron flow, sub-Alfvénic ion outflow, and magnetized electron outflow within the exhaust layer. The electron dynamics in the outer EDR can affect the opening angle, thus, the reconnection rate. In this event the opening angles were calculated (magnetosphere side $\phi = 24^{\circ} \pm 4^{\circ}$, magnetosheath side $\theta = 6^{\circ} \pm 4^{\circ}$)

between magnetospheric and magnetosheath plasmas (Chang et al. 2021; Graham et al. 2017).

The interaction between inflow and outflow can also generate electron vorticity in the separatrix layer (Ahmadi et al. 2022). Such vortices and current loops can induce magnetic field disturbances (Hwang et al. 2019; Stawarz et al. 2018). However, in the magnetospheric separatrix, the net potential of spiky structures is not enough to accelerate the observed electron inflows. Instead, the spiky structures contribute to a rapid electron-time-scale thermalization of plasmas that are transported into the magnetospheric inflow region by ion-scale lower-hybrid drift waves (Holmes et al. 2019). These heating processes engaging multi-scale waves can lead to pre-heating of inflowing plasmas before they enter the EDR.

Beyond this coupling of kinetic reconnection boundaries, the global-scale characteristics of the X-line as well as evolution and consequences of multiple X-lines developed on the dayside magnetopause are discussed in the following Sects. 3.3 and 3.4, respectively. The multi-scale processes and structures occurring in the exhaust region are detailed in Sect. 3.4.

3.3 Extent of Reconnection X-Lines and 3D Complexities

When the IMF is southward, magnetic reconnection at the magnetopause occurs at relatively low latitudes between magnetic field lines in the magnetosheath and field lines in the magnetosphere. This reconnection produces long, continuous, quasi-stationary X-lines that can extend across the entire dayside and possibly along the flanks of the magnetopause. These conclusions about reconnection X-lines were developed from multi-spacecraft observations at the magnetopause (e.g., Dunlop et al. 2011; Phan et al. 2000), global auroral imaging (Fuselier 2002), observations in the magnetospheric cusps (Trattner et al. 2021a, 2007) and,

more recently, observations from the MMS mission (Fuselier et al. 2019b; Hasegawa et al. 2016; Trattner et al. 2021b).

Recent MMS observations indicate that X-line length appears to depend on where reconnection is occurring at the magnetopause and whether there is a guide field at the X-line (Fuselier et al. 2021). Together with the outflow velocity data, multi-species ion distributions imply the location of X-line and magnetic topology (Fuselier et al. 2019a; Petrinc et al. 2020). These recent observations also indicate that the orientation of X-lines at the magnetopause is also a complicated function of these two conditions. Figure 7(a) shows the shear angle between the draped magnetosheath and the magnetospheric field lines at the magnetopause. High (low) magnetic-shear regions are shown in red (blue/purple). These magnetic shear angles at the magnetopause are projected onto the Y-Z plane in GSM. Figure 7(a) depicts the magnetic shear conditions when MMS was at the magnetopause on 22 January 2017 and the IMF (brown vector in the lower right) was strongly southward with a duskward component. Under these conditions, the maximum magnetic shear model (Trattner et al. 2007, 2021b) predicts that there is a more-or-less continuous reconnection X-line that stretches from the dawnside along a “ridge” of oppositely-directed (anti-parallel) magnetosheath and magnetospheric field lines. The X-line cuts across the noon meridian ($Y_{\text{GSM}} = 0$), forming the component X-line in Fig. 7. This component X-line connects the two anti-parallel ridges on the dawnside and duskside. Anti-parallel reconnection occurs along the ridges, where the shear is 180° and component (or guide field) reconnection occurs along the “component X-line” that cuts across the noon meridian where the shear is $<180^\circ$.

The orientation of the X-line is different for the component X-line and for the anti-parallel X-lines. Fuselier et al. (2021) investigated the X-line orientations for 37 events where the MMS spacecraft were at or very close to the X-line. The X-line is oriented along the M direction in the standard LMN coordinate system at the magnetopause. Figure 7(b) shows that the component X-line is oriented along the M direction. This orientation implies that the component X-line is many R_E long and continuous. Crossings anywhere along this X-line show the same orientation.

For the anti-parallel X-lines on the duskside and dawnside, the orientation and the length of the X-lines are different from the component X-line. The X-lines are oriented perpendicular to the anti-parallel ridge in the region between the “knee” in the ridge and the component X-line as shown in Fig. 7(c). This orientation implies that this part of the anti-parallel X-line is actually composed of short ($\sim 1 R_E$) X-lines that are stacked as stairsteps along the ridge. Along the anti-parallel ridge from the knee to the beyond the dawn terminator, the X-line is oriented along the ridge.

Thus, the length of the X-line depends on the location at the magnetopause and on the magnetic shear angle where reconnection occurs. While the maximum shear model predicts the extent and orientation of X-lines over the entire magnetopause surface, PIC simulations (Liu et al. 2018b) showed that when a primary X-line misaligns with the optimal orientation due to, e.g., time-varying upstream conditions, secondary X-lines develop to adjust the orientation. Such multiple X-lines, similar to Fig. 7(c), may facilitate the formation of flux ropes and/or secondary islands, which is discussed in Sect. 3.4.

3.4 Flux Ropes and Flux Transfer Events (FTEs)

The flux ropes formed on the surface of the magnetopause, termed flux transfer events (FTEs), are the manifestation of cross-scale or multi-scale aspects of magnetopause reconnection. The observational phenomena of these structures include a bipolar signature in the magnetic field component normal to the nominal magnetopause (B_N), an increase or decrease in the magnetic field strength at (or bounding, in the case of crater FTEs) the center

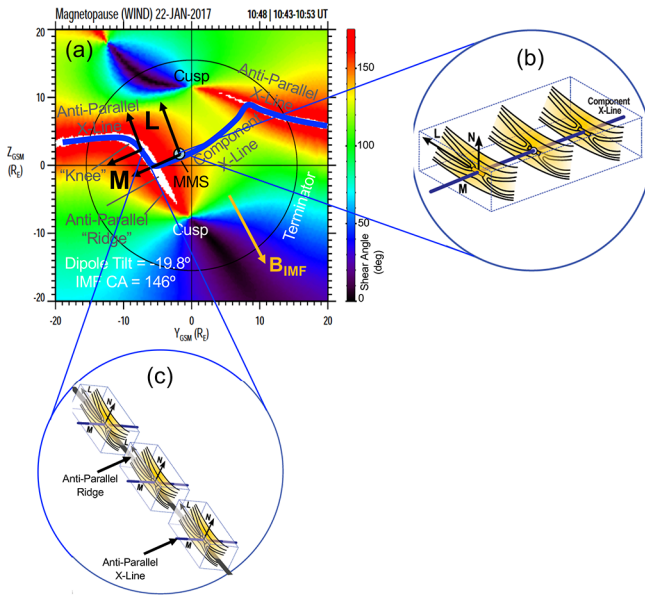


Fig. 7 Shear angle between the magnetosheath and magnetospheric magnetic fields at the magnetopause projected onto the Y-Z_{GSM} plane (a). These shear angles are for 22 January 2017 at 1048 UT when MMS was at the magnetopause and the IMF was strongly southward with a duskward component. The thick blue line traces out a continuous X-line stretching from the dawn flank to the dusk flank magnetopause. The orientations of X-lines are determined by the M direction in the LMN coordinate system. The component X-line is long and continuous and crossings of this X-line show the same orientation of the reconnection structure (b). Part of the anti-parallel ridge is composed of short X-lines that are oriented perpendicular to the ridge (c)

of the B_N reversal, and coexistence of the magnetospheric and magnetosheath plasma inside the FTE.

These characteristics of FTEs are explained by their generation mechanisms invoking 1) transient bursts (spatially and temporally) of dayside reconnection (Russell and Elphic 1978), 2) the turn-on-and-off or temporal modulation of the reconnection rate of single X-line reconnections (Phan et al. 2004; Scholer 1988; Southwood et al. 1988), or 3) multiple X-lines (in 2-D representations) or separator lines (in 3-D representations) (Lee and Fu 1985; Scholer 1995). Different generation mechanisms necessarily give rise to different magnetic topologies or magnetic field connectivities within and around the FTEs.

MMS with its high-resolution measurements enabled us to resolve the detailed substructures of FTEs: multi-layered substructures within a crater FTE (Hwang et al. 2016); reconnecting current sheets between interlinked flux tubes (Kacem et al. 2018; Kieokaew et al. 2020; Øieroset et al. 2019; Hwang et al. 2020b); electron-scale reconnecting current sheets at the leading edge of an FTE or a flux rope (Poh et al. 2019; Zhong et al. 2021); electron- or ion-scale current layers at the interface of two coalescing FTEs (Wang et al. 2017; Zhou et al. 2017); and ion-scale flux ropes growing from an electron-scale current layer (Hasegawa et al. 2023).

Figure 8(b-e) show the observations of a series of the ion-scale FTEs (marked by shaded areas) when MMS crossed between the low-latitude boundary layer (LLBL; green bar at the top of panel b) and the magnetopause current sheet (red bar). Four-spacecraft measurements allow the force analysis across FTEs: the magnetic tension force (Fig. 8c) is relatively

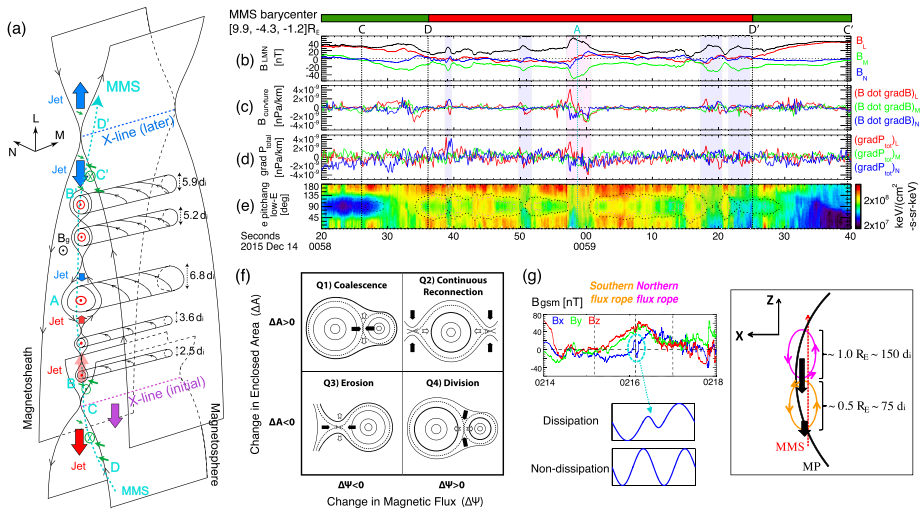


Fig. 8 Adopted from Hwang et al. (2018), Zhou et al. (2017), and Akhavan-Tafti et al. (2020). The observation of a series of ion-scale FTEs generated in the magnetopause current sheet (a-e): across FTEs the magnetic tension force (c) is relatively balanced by the total pressure gradient force (d). The relative motion between the initial and later X-lines (a) facilitates the formation of FTEs via tearing instability. These FTEs can interact via reconnection which dissipates the magnetic field at the interface of the two flux ropes to coalesce (g)

balanced by the total pressure gradient force (Fig. 8d). Throughout the current sheet, the low-energy electrons consist of two populations (Fig. 8e): a field-aligned population accelerated by the electrostatic potential (Egedal et al. 2008) and a trapped (centered on 90° pitch angles) population locally bouncing within the reconnection exhaust (Lavraud et al. 2016). Both indicate ongoing reconnection around the FTEs.

Figure 8(a) illustrates the MMS trajectory (cyan dashed arrow) across these small-scale FTEs. The relative drift between the initial and later X-lines facilitates the formation of multiple secondary islands or FTEs via tearing instability. These FTEs can interact with each other or the ambient magnetic field to either coalesce (Fig. 8g) or erode. Simulation studies by Akhavan-Tafti et al. (2020) predicted the Fig. 8(a-e) FTEs to grow Earth-sized within 10 min, and continuous reconnection at adjacent X-lines between FTEs is the dominant source of magnetic flux and plasma of the resulting large-scale FTEs. Possible interactions between flux ropes and the resulting magnetic geometry are summarized in Fig. 8(f) in terms of the change in the enclosed area inside an FTE and its magnetic flux content (Akhavan-Tafti et al. 2020). These studies indicate that microscale (electron) and mesoscale (ion) processes associated with reconnection occurring around FTEs play a crucial role in the generation, structure, and evolution of FTEs, which, in turn, modulate the structure and evolution of pre-existing or primary reconnection.

Formation and evolution of FTEs are directly linked to magnetic field connectivity with Earth’s magnetosphere, affecting solar wind mass, momentum, and energy transfer into the magnetosphere down to the ionosphere. Implications of these FTEs on the large-scale magnetosphere-ionosphere coupling (MIC) processes are obtained from the sequential observations of FTEs, poleward moving auroral forms, and polar cap patches (Hwang et al. 2020b).

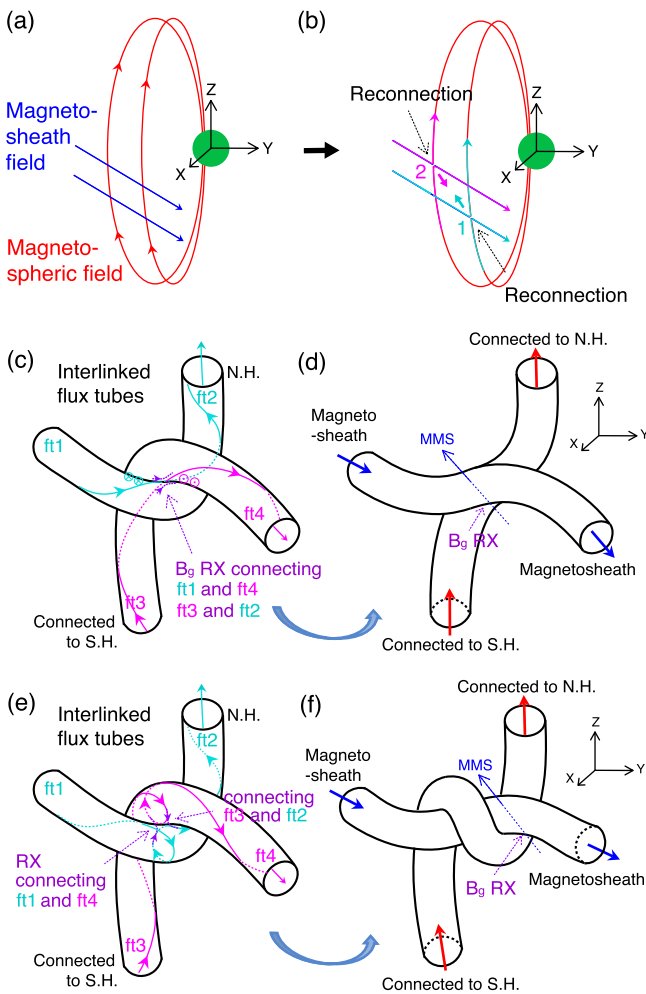


Fig. 9 Adopted from Hwang et al. (2021). Interlinked flux tubes form via multiple reconnection X-lines (a-b-c, a-b-e). Two reconnected flux tubes interact at the center of the interlinked flux tubes via localized reconnection (c, e). Resultant structures keep evolving their magnetic connectivity (d, f). This entanglement can suppress the tailward transition of this type of FTEs

MMS identified the generation and evolution of interlinked flux tubes. Figure 9 shows how the interlinked flux tubes can form and evolve via localized reconnection, which necessarily entails the change of the magnetic connectivity. Figure 9(a, b) illustrate the generation of interlinked flux tubes under the southward IMF with a significant B_y component. This condition leads to two X-lines developed on the dayside magnetopause, and two reconnected flux bundles collide with and entangle each other. A notable difference in the energy-dependent electron pitch-angle distributions before and after the center of the flux rope/FTE indicates such interlinked flux tubes (Hwang et al. 2021; Kacem et al. 2018; Russell and Qi 2020)

At the interface of the two flux tubes (Fig. 9c, e), converging jets together with the magnetic pile up (Øieroset et al. 2016; Øieroset et al. 2019; Maheshwari et al. 2022) lead to

the formation of a compressed current sheet giving rise to the onset of reconnection (Fargette et al. 2020). As a result, the two flux tubes change their connectivity either with both ends connected to the magnetosphere or with both ends connected to the magnetosheath (Fig. 9d, f). Furthermore, reconnection at the leading edge of FTEs between the FTE field lines and the magnetospheric (closed), magnetosheath (unconnected), or boundary layer (open or complex topology) field lines will affect whether FTEs significantly contribute to nightside flux transport or not, as will be different for loosely- vs. tightly-interlinked flux tubes (Fig. 9d vs. 9f). These scenarios indicate that the localized physics occurring in FTEs can make macroscopic impacts such as the global circulation of magnetic flux through the magnetosphere and solar wind-magnetosphere coupling, affecting the content and rate of the magnetic flux and solar wind transfer.

Mejnertsen et al. (2021) studied the propagation, evolution, and fate of FTEs generated by multiple reconnection X-lines. They simulated a real solar wind event using the MHD code to find that 1) the extent to which FTEs add magnetic flux to the tail depends on their topology and 2) the resulting FTEs transit around the flankside magnetopause before they eventually dissipate due to non-local (nightside magnetotail) reconnection altering the FTE topology. The FTEs drifting on the flanks of the magnetopause also affect local dynamics occurring there that typically involve velocity-shear driven multi-scale processes, which is the topic of Sect. 4.

4 Reconnection in the Flankside Magnetopause

4.1 Introduction

Figure 5(c) represents the reconnection geometry typically occurring on the flank-side magnetopause. The combined flow shear and density asymmetry have multiple effects on reconnection such as the drift of the X-line (Fig. 5c) and the reconnection efficiency (Cassak and Otto 2011; Doss et al. 2015). These combined effects also drive an additional asymmetry in the reconnection exhaust region (La Belle-Hamer et al. 1995). In the upper (tailward) exhaust of Fig. 5(c), the outflow is in the same direction as the upstream magnetosheath flow. A smaller force is required to drive the outflow. On the other hand, the larger density on the magnetosheath side requires a larger accelerating force to drive the outflow. Thus, the effects of shear flow and density gradient compete on one side but enhance each other on the other side. The tailward exhaust, where the two effects compete, exhibits a broader magnetic field transition region often bounded by bifurcated current sheet. The sunward exhaust, where the two effects enhance each other, becomes a narrow current sheet with the accelerated flow entrained toward the magnetospheric side.

Tanaka et al. (2010), using PIC simulation codes, studied the effects arising from the combination of a guide field as well as a flow shear in density-asymmetric reconnection. They showed that both an initial upstream flow and the Lorentz force acting on inflowing plasmas due to a guide field produce a slanted inflow to the current sheet, giving rise to asymmetries in the quadrupolar exhaust similar to the MHD simulation by La Belle-Hamer et al. (1995). The MMS observation reported by Hwang et al. (2021) indicated the predicted quadrupolar reconnection current layer with asymmetric exhaust patterns. Tanaka et al. (2010) also showed that the X-line motion is controlled either by the ion flow when the shear flow effects dominate or by the electron flow when the guide field effects dominate, as well as the development of asymmetric exhausts.

These studies considered the case where the velocity shear co-exists with the magnetic shear in the reconnection plane. Although this is a valid case for high-latitude dayside reconnection as well, the intrinsic difference of flankside reconnection comes from the fact that Kelvin-Helmholtz instability (KHI) driven by fast magnetosheath shear flows efficiently compresses the magnetopause current sheet, facilitating the onset of reconnection (details in Sect. 4.2).

Furthermore, under mostly southward IMF the current sheet configuration on the flankside magnetopause is typically a largely antiparallel magnetic field with a perpendicular shear flow (Fig. 1 of Ma et al. 2014a). In this case, both reconnection and KHI can simultaneously operate. In the linear stage, the initial perturbations (magnetic shear vs. flow shear) determine the primary process. In the nonlinear stage, the two modes interact with each other: for the case of initially dominant KHI, reconnection is driven and strongly modified by nonlinear KH waves, producing complex flux ropes via patchy reconnection (Ma et al. 2014b, 2014a); for the case of initially dominant reconnection, the onset of reconnection causes a thinned shear flow layer, generating small wavelength KH waves, which in turn modulate the diffusion region and increase the reconnection rate (Ma et al. 2014b).

Reconnection can also occur out of the shear plane due to a 3-D twist of magnetospheric and magnetosheath magnetic fields induced by KH vortices (Sect. 4.3). This section lastly addresses an important question concerning mass transport, i.e., solar wind entry across the flankside magnetopause and plasma mixing in the LLBL induced by KHI-driven reconnection (Sect. 4.4).

4.2 In-Plane 2-D Reconnection in the Presence of a Velocity Shear

When the velocity shear exists in the same 2-D plane as the reconnection plane, the linear growth of the tearing instability is stabilized by the velocity shear (e.g., Chen and Morrison 1990). However, when the shear flow speed V_0 exceeds the Alfvén speed based on the magnetic field component parallel to the velocity shear ($V_0 > V_A$), the KHI becomes unstable overcoming the in-plane magnetic tension (e.g., Chandrasekhar 1961; Miura and Pritchett 1982).

Numerical simulations treating non-linear physics of the KHI demonstrated that under such super-Alfvénic conditions the vortex flow produced by the non-linear growth of the KHI can locally compress the pre-existing magnetic shear layer (current sheet), and secondarily induce reconnection (Knoll and Chacón 2002; Nakamura et al. 2006, 2011; Pu et al. 1990), as shown in Fig. 10(a). This process is termed vortex-induced reconnection (VIR) or the Type-I VIR (Nakamura et al. 2008). Note that when the KHI produces highly rolled-up vortex arms, which can form with a strong velocity shear in a range of $V_0 > 2-3 V_A$ (Miura 1984; Nakamura and Fujimoto 2005), the highly-swirled magnetic field lines involved within the arms can newly form thin secondary current sheets and induce reconnection (Faganello et al. 2008; Nakamura and Fujimoto 2005; Nykyri and Otto 2001). This type of VIR is categorized as Type-II VIR (Nakamura et al. 2008).

It is notable that the VIR can be triggered even when the initial shear layer is too thick to cause fast spontaneous reconnection, because the non-linear vortex flow rapidly compresses the thick layer down to electron-scales (Nakamura et al. 2008, 2011) (Fig. 10a). Indeed, evidence of VIR has been reported at the Earth's dayside-to-flank magnetopause (Eriksson et al. 2016; Hasegawa et al. 2009; Hwang et al. 2020a; Nakamura et al. 2013) whose thickness is typically of the order of 10^3 km and larger than ion-scales (e.g., Berchem and Russell 1982). It is also notable that the rate of VIR is basically higher than that of regular reconnection since the super-Alfvénic vortex flow produces a strong inflow towards the

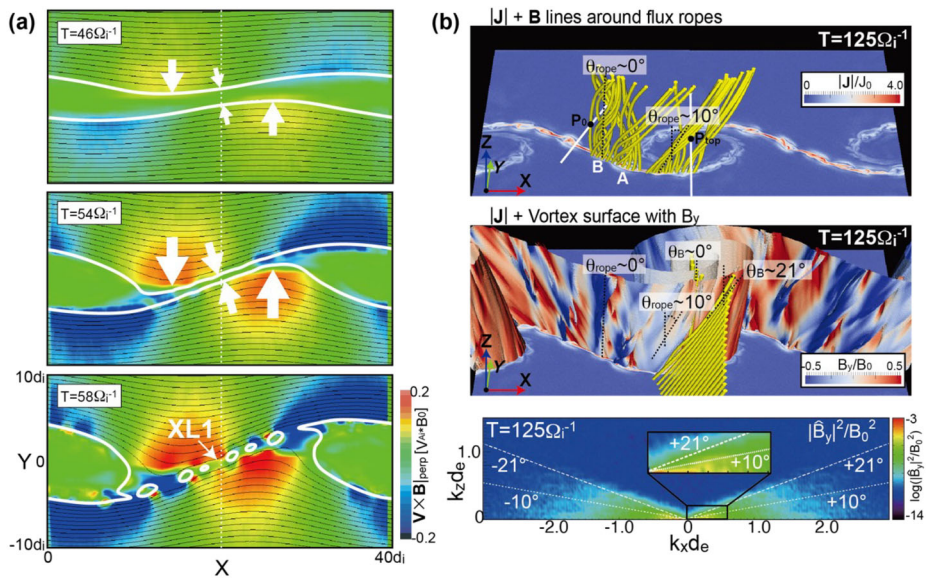


Fig. 10 (a) Time evolution of the perpendicular component of the convection electric field and two selected magnetic field lines in a 2-D fully kinetic simulation, showing the onset of VIR and resulting magnetic island (flux rope) formation in the compressed current sheet (adopted from Nakamura et al. 2011). (b) 3-D views of (top) selected field lines near the VIR-produced transverse/oblique flux ropes and (middle) the vortex surface with the reconnected field component B_y , and (bottom) corresponding magnetic power spectrum (k_x, k_z) in a 3-D fully kinetic simulation, showing the 3-D evolution of VIR and resulting flux ropes over a broad range of oblique angles (adopted from Nakamura et al. 2013)

VIR region (Nakamura et al. 2011). Namely, VIR is a kind of strongly-driven reconnection process, which has been less explored in the reconnection physics. This process results in an efficient plasma mixing and transport across the shear layer along the reconnected field lines (Nakamura et al. 2011).

Recent 3-D kinetic simulations of VIR also demonstrated that the VIR can be triggered at more than one sites in 3-D, with X-line orientations distributed over the entire range of angles between the field direction on one side and that on the other side. As a result, multiple oblique flux ropes are formed along the vortex surface (Fig. 10b), which further enhances the rate of the mass transfer (Nakamura et al. 2013, 2017b).

MMS has provided observational evidence of VIR-generated flux ropes. Figure 11 shows MMS observations of a flux rope locally generated at the KH vortex boundary (Hwang et al. 2020a; Kieokaew et al. 2020). Both outer-leading (‘O-L’) and outer-trailing (‘O-T’) edges of the flux rope exhibit reconnection signatures including flow reversals (blue arrows in Figure 11Ab, c). This is consistent with the prediction from the Grad-Shafranov reconstruction of the magnetic field (Fig. 11Ba, b; see details in Hasegawa et al. 2023). The magnetic-field map (black contours) demonstrates an elongation of the flux rope associated with ion flows converging toward the FTE center (colored arrows in Fig. 11Ba). Both plasma flow and density patterns (Fig. 11Ba, b) are consistent with the flux rope generated by VIR (Fig. 10).

At the center of the B_N reversal (marked by vertical dashed black lines, ‘C’ on the top of Fig. 11A), the rapid B_N change across ‘C’ with a dip in the magnetic field strength (black profile in Fig. 11Aa; blue in Fig. 11Ad) indicates the existence of local reconnection at the FTE center, as evidenced by ion outflow jets (red arrow in Fig. 11Ab) and out-of-plane

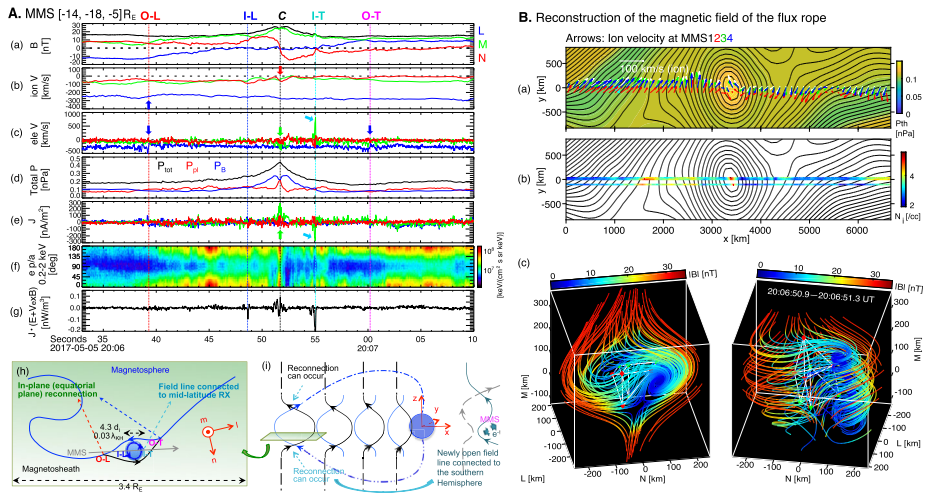


Fig. 11 A. A flankside FTE observed by MMS: (a) the magnetic field, \mathbf{B} (LMN components and B); (b, c) ion and electron bulk velocities; (d) the plasma (red; P_{pl}) and magnetic (blue; P_B) pressures, and the sum of P_{pl} and P_B (black); (e) the electric current density; (f) the pitch angle distribution for electrons of 0.2–2 keV energy; (g) the energy conversion rate in the electron frame ($\mathbf{J} \cdot \mathbf{E}'$); illustration of VIR-driven flux rope generation (h) and the onset of mid-latitude reconnection (i; Sect. 4.3). Inner-leading (trailing) and outer-leading (trailing) edges are denoted by ‘I-L’ (‘I-T’) and ‘O-L’ (‘O-T’), respectively. B. Reconstruction of the magnetic field of the flux rope shown in panels A(a-h) using the Grad-Shafranov (a, b) and SOTE (c) reconstruction methods. Adopted from Hwang et al. (2020a)

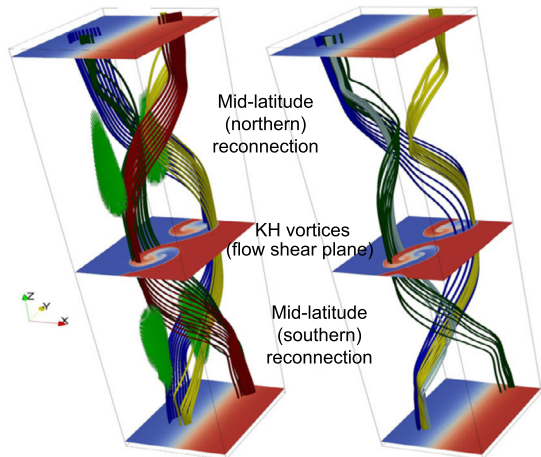
current-carrying electron jets (green arrow in Fig. 11Ae), non-zero $\mathbf{J} \cdot \mathbf{E}'$ (Fig. 11Ag), and electron agyrotropy (not shown; Hwang et al. 2020a). Polynomial or second-order Taylor expansion (SOTE) reconstruction methods (Denton et al. 2020; Liu et al. 2019) present an interlinking of two flux tubes (Fig. 11Bc; Sect. 3.4). Indeed, MMS observed notable difference in the electron pitch angle distribution across ‘C’ (Fig. 11Af) and strong magnetic tension force toward the FTE center (not shown).

The Fig. 11 event demonstrates that reconnection occurs at diverse locations on a variety of scales within the KH vortex, suggesting that KHI and reconnection cooperate on the plasma transport and mixing across the flank magnetopause. 3-D PIC simulations (Nakamura and Daughton 2014; Nakamura et al. 2017a) showed that the rate of the VIR-produced mass transfer across the flank magnetopause, such as the diffusion coefficient ($D_{diff} \sim 10^{10-11}$ m²/s), could be one-to-two orders of magnitude higher than the previously predicted rate ($D_{diff} \sim 10^9$ m²/s; Nykyri and Otto 2001) to form the LLBL where the solar wind and the magnetospheric plasmas are mixed. These results indicate that the multi-scale evolution of the VIR may crucially contribute to large-scale mass transfer across the boundary layer where the magnetic and velocity shears co-exist such as the Earth’s magnetopause.

4.3 Mid-Latitude Reconnection, Associated 3D Magnetic Topologies

Figure 11A exhibits a distinctive out-of-plane (northward in this event) electron jet at the inner-trailing edge (‘I-T’) of the flux rope (Fig. 11Ac), carrying most of the current (Fig. 11Ae). The field-aligned jet was not consistent with acceleration by the local electric field, leading to negative $\mathbf{J} \cdot \mathbf{E}'$ (Fig. 11Ag). Observed open field-line topology (illustrated in Fig. 11i) further indicated that the magnetic field lines at ‘I-T’ might be connected to

Fig. 12 Adapted from Faganello et al. (2012). Left frame: blue/red colors show tracers of the original side of each field line in the simulations, at the equator and two mid-latitude (X, Y)-planes, light green shows current isosurfaces of large currents, and selected field lines of various colors show the complex magnetic topologies that arise. Right frame: at a later time in the simulation, the green ochre, and grey field lines show pristine magnetospheric, and once-reconnected and double-reconnected field lines, respectively



mid-latitude reconnection between twisted field lines of magnetosheath (black curves in Fig. 11Ai) and magnetosphere (blue) origin in the southern hemisphere.

Thus, in addition to Type-I and Type-II VIR triggered within KH vortices (Sect. 4.2), reconnection can also occur at mid-latitudes in association with the 3-D growth of the KHI. The fact that this type of reconnection is different from VIR occurring in the velocity shear plane is clearly illustrated in Fig. 12 from Faganello et al. (2012).

For the purely northward IMF case as simulated for Fig. 12, Type I and II reconnection would occur in association with the main vortex development in the equatorial plane. Mid-latitude reconnection, by contrast, is triggered away from the equatorial plane as a result of the relative flow shears at the two locations, producing magnetic shears at mid-latitudes that are prone to the triggering of reconnection. The twisting of magnetic field lines as induced by this process also has impacts on coupling to the ionosphere, i.e., the generation of field-aligned currents (e.g., Hwang et al. 2022; Johnson and Wing 2015; Johnson et al. 2021; Petrincic et al. 2022). Mid-latitude reconnection can relax the 3-D twist of the field lines, thus, affecting the large-scale MIC.

Borgogno et al. (2015) studied in further detail the changes in the global magnetic topologies that result from this process in 3-D. They showed in particular that field lines can be reconnected in different ways as the process evolves in the simulation. Magnetic field lines in the simulation domain are found to be reconnected at either one or both reconnection regions at mid-latitudes, with occurrence rates evolving over the time (cf. Faganello et al. 2022; Sisti et al. 2019). Using high-resolution MMS data, Vernisse et al. (2016) showed in-situ signatures of the mid-latitude reconnection process. The observations further suggested that both mid-latitude reconnection (in both hemispheres) and Type-I VIR in the equatorial plane may be occurring at the same time. A direct implication of this possibility is that magnetic field topologies can be even more complex than suggested by Borgogno et al. (2015) since the possible magnetic topologies then become a combination of not only two but three reconnection regions for the same field lines (Type-I or Type-II reconnection in the equatorial plane and the two reconnection regions at mid-latitudes in the northern and southern hemispheres). This is illustrated in Fig. 13, where the various possible combinations are sketched.

Further simulations by Fadanelli et al. (2018), using non-purely northward IMF conditions, showed that in such cases the whole geometry of the KH process is skewed: the distinction between reconnection in the equatorial plane and at mid-latitudes is not clear

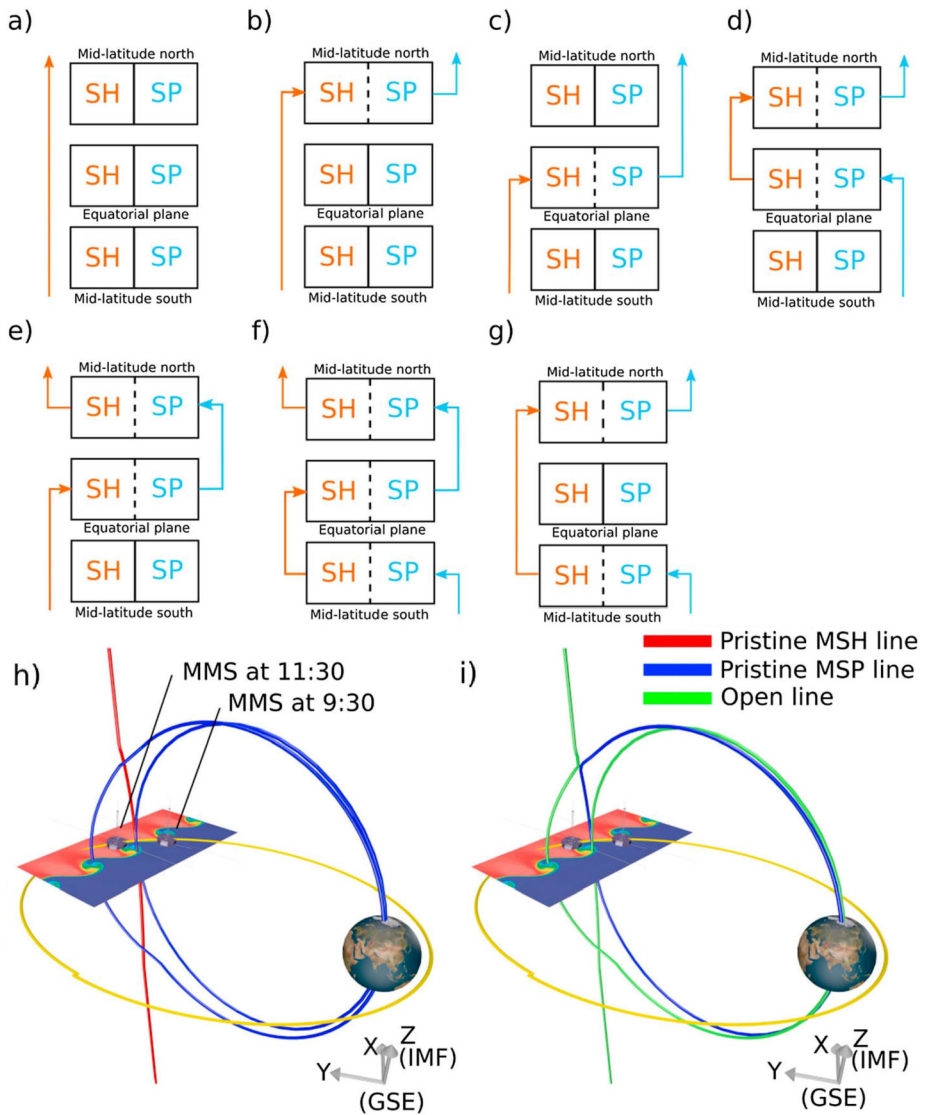


Fig. 13 Adopted from Vernisse et al. (2016). (a–g) Possible topologies of a field line observed on the magnetosheath side of a wavy magnetopause induced by the KHI. SH corresponds to the magnetosheath side and SP to the magnetosphere side. A dashed line within the rectangle between the SH and SP parts means that reconnection is occurring at this particular site. A solid line within the rectangle signals that the magnetopause is closed at this site. (h and i) Example of field line changing topology. Two closed magnetospheric field lines (blue) and one magnetosheath field line (red) before (h) and after (i) reconnection has occurred in the local KH wave and at midlatitude in the northern hemisphere. The resulting open field line is depicted in green

anymore, such that there exists a broad region of possible reconnection from mid-to-low latitudes in one of the hemispheres. The fact that reconnection sites may occur over a broad range of latitudes was later confirmed with MMS observations by Vernisse et al. (2020). Also, similar or even more complex features were found in simulations by Sisti et al. (2019)

or Faganello et al. (2022). For the specific conditions of the MMS KHI event on 8 Sep 2015 (cf. Eriksson et al. 2016; Vernisse et al. 2016), the late nonlinear phase of the KHI simulation (Faganello et al. 2022) showed the development of broad regions of reconnection and vortex pairing at all latitudes. They also found that secondary KHI develops, but only in the northern hemisphere, leading to an enhancement of the occurrence of off-equator reconnection, which is also consistent with observations by Vernisse et al. (2020).

In a symmetric configuration between the northern and southern hemispheres described in Faganello et al. (2012), the double mid-latitude reconnection process with an equal occurrence and rate does not provide a net transport of mass. Under asymmetric conditions, however, transport may occur and be quantified. For such asymmetric conditions Ma et al. (2017) identified doubly-reconnected field lines and estimated the mass transport rate to be on the order of 10^{10} m²/s, comparable to the VIR-produced mass transport rate (Nakamura and Daughton 2014). The importance of KHI for mass transport into the magnetosphere is now well established, as addressed in a review by Faganello and Califano (2017), which also describes in more details the roles of magnetic reconnection in association with the instability. We further discuss this topic in Sect. 4.4.

4.4 Plasma Mixing, Transport, and Turbulence

Magnetic reconnection induced by the nonlinear development of the KHI at the flank magnetopause has been invoked to have cross-scale or large-scale impacts, including turbulence generation, plasma mixing in KH vortices, and plasma transport across the magnetopause and possibly into the near-Earth portion of the magnetotail. Stawarz et al. (2016) reported a magnetic power spectrum with a power-law index $-5/3$, namely, a traditional Kolmogorov-type turbulence feature at the MHD scale, for the 8 Sep 2015 event of magnetopause KH waves with reconnection jet signatures (Eriksson et al. 2016). Interestingly, a 3-D fully kinetic simulation of this MMS event showed that VIR in 3-D can generate such a turbulent power spectrum even in an early nonlinear stage of the KHI (Nakamura et al. 2017b). Consistently, a study by Hasegawa et al. (2020), in which the same MMS event was compared with a dayside magnetopause crossing event without KHI activity, suggested that magnetic turbulence can be enhanced as a consequence of the KHI growth. Notably, the cross-scale energy transfer rate was shown to be larger on the magnetospheric side of the KH-unstable magnetopause, where the turbulence level was low initially but VIR may grow more vigorously, than on the magnetosheath side where turbulence may be already developed (Quijia et al. 2021). [See Stawarz et al., this collection, for further discussion on an interplay between the KHI, VIR, and turbulence.]

The simulation by Nakamura et al. (2017b) also showed that in a fully developed phase of the KHI and thus of VIR, the rate of particle entry across the magnetopause per one KHI wavelength can be of order 10^{26} s⁻¹ and a dense LLBL of ~ 1 R_E thickness can form around the dawn-dusk terminator (Nakamura et al. 2017a). The study thus suggests that VIR significantly contributes to plasma mixing across the flank magnetopause and the LLBL formation. A question from the viewpoint of macroscale impact is then whether LLBL plasmas could be transported beyond the boundary layer into the central or midnight portion of the magnetotail through the KHI or VIR.

Figure 14 shows energy-dispersed ion beams at energies less than 1 keV (thus most likely of magnetosheath origin) observed by MMS in the duskside plasma sheet during a northward IMF period. Nishino et al. (2022) applied both time-of-flight (Lockwood and Smith 1989) and pitch-angle dispersion analyses (Burch et al. 1982) to the observed field-aligned and anti-field-aligned ion beams in order to estimate the source location of these

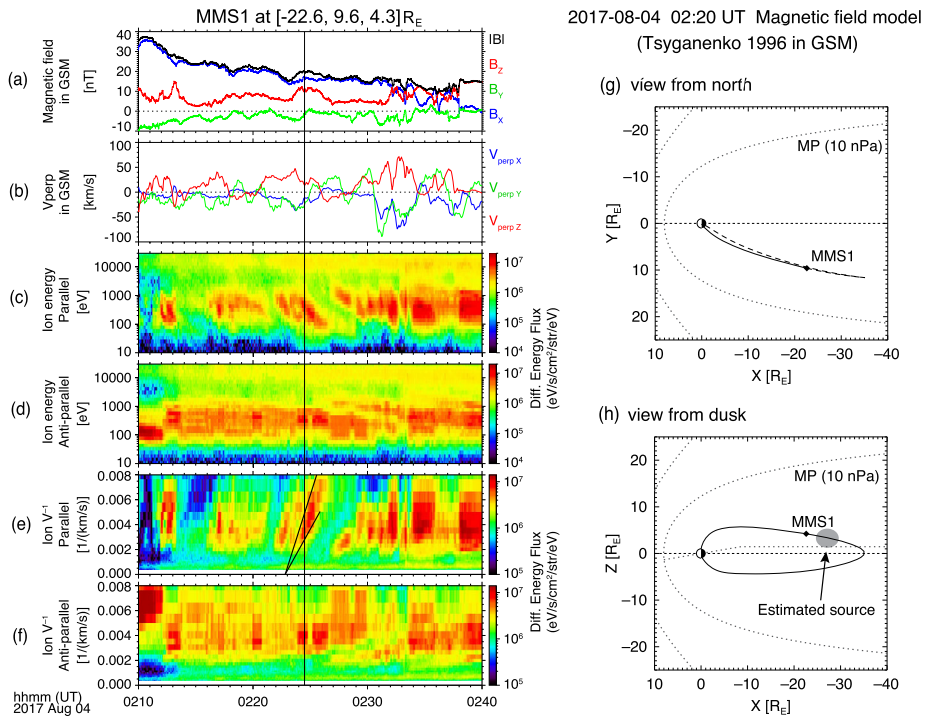


Fig. 14 Adopted from Nishino et al. (2022). MMS observations of repeated energy dispersed magnetic-field-aligned ion beams in the duskside magnetotail during northward interplanetary magnetic field conditions. Panels (c) and (d) show fast and slow dispersions, respectively, consistent with source locations of the beams on the tailward and dusk side of MMS, which may well be a dusk-flank boundary layer where vortex induced reconnection can occur (g, h). Time-of-flight analysis (e) suggests a distance to the source region of $\sim 5 R_E$

ions. The results show that under the observed solar wind conditions, they can be traced back to a dusk-flank boundary layer at a distance $\sim 5 R_E$ on the tailward and dusk side of MMS. Interestingly, the field-aligned (earthward traveling) energy-dispersed ions were observed repeatedly with a recurrence time of order a few min (Fig. 14c), which is similar to the KH wave period in the tail flanks (e.g., Hasegawa et al. 2006). This suggests their possible connection to KHI activity; magnetic reconnection induced in a KH-active flank boundary layer may have injected cool ions of magnetosheath origin toward the near-Earth plasma sheet. Their results indicate that, in addition to poleward-of-the-cusp reconnection in both northern and southern hemispheres (e.g., Li et al. 2008), VIR may play a role not only in plasma transport across the magnetopause and mixing in the LLBL but also in large-scale plasma transport, namely, the formation of the cold-dense plasma sheet under northward IMF (Terasawa et al. 1997).

Another aspect from the viewpoint of cross-scale processes is that velocity fluctuations or turbulence in the magnetosheath, which can act as seeds for the KHI and thus VIR, are generally more intense on the dawn than dusk side (e.g., Nykyri et al. 2017). In the presence of such magnetosheath turbulence, larger KH vortices can grow, leading to larger-scale and faster plasma transport (Nakamura et al. 2020; Nykyri et al. 2017). Resulting dawn-dusk asymmetric transport may be responsible, at least partially, for dawn-dusk asymmetries in the plasma sheet density and ion spectra (Wing et al. 2005).

When the plasma and magnetic fluctuations caused by KHI-associated reconnection at the flank magnetopause penetrate toward the midnight region, they provide perturbations in the central tail current sheet that can modify background parameters around the reconnecting current sheet and/or possibly serve triggers of the marginally stable current sheet in the central plasma sheet. Section 5 discusses multi-scale dynamics of reconnection occurring in the magnetotail.

5 Reconnection in Nightside Magnetotail

5.1 Introduction

The background magnetotail current sheet is generally symmetric between the northern and southern hemispheres across the current sheet with no or only small guide field compared to dayside boundaries. Instead, the magnetotail current sheet is asymmetric along the magnetotail axis bounded between the hotter plasma population trapped by Earth's dipole field in the inner magnetosphere at the earthward side and the solar wind plasma on the wake side (tailward side).

Magnetotail reconnection is expected to have, therefore, nearly 2-D geometry locally around the diffusion region in the first place. Corresponding scale sizes for EDR and IDR in the terrestrial magnetotail are on the order of d_e ($d_e < 40$ km) and d_i ($d_i < 1600$ km), respectively. The reconnection X-line is most likely to be localized with an extent of a few R_E in the magnetotail as inferred from the localized cross-tail (dawn-dusk) scales of fast plasma flows, called bursty bulk flows (BBFs; Angelopoulos et al. 1992), about one order smaller than the magnetotail dimension. Hence the evolution and consequence of the reconnection propagating from localized reconnection sites involve 3-D and transient processes, producing complex multi-scale structures.

One of the most important consequences of the energy transport from the reconnection site is a variety of instabilities in the transition region from tail-like to dipolar magnetic fields. In this region the reconnection jets brakes and/or diverts and energy is deposited to the ionosphere (Fuselier et al., this collection) as well as energetic particles are injected toward the inner magnetosphere (Oka et al., this collection).

In the following we highlight recent advances in our understanding of the multi-scale disturbances beyond the diffusion regions (Norgren et al., Genestreti et al., Liu et al., this collection) that are connected to the large-scale magnetotail processes (Fuselier et al., this collection). We focus on the onset (Sect. 5.2), evolution (Sect. 5.3), and consequences (Sect. 5.4) of magnetotail reconnection.

5.2 Onset Conditions for Local/Global Current Sheet Thinning

Formation of the thin current sheet during substorm growth phase (before the onset of reconnection) takes place due to the magnetic flux accumulation in the lobe (Birn and Schindler 2002) and/or enhanced loss of the closed magnetic flux toward the dayside magnetosphere (Hsieh and Otto 2014). Both processes are due to enhanced dayside magnetopause reconnection (Fuselier et al., this collection).

Cluster, THEMIS, and MMS observations in the region between 10–25 R_E , where the near-Earth reconnection takes place, showed that the thin current sheet is embedded in a thicker plasma sheet in stretched magnetic field configuration with a small B_Z (normal) component (Artemyev et al. 2021, 2016; Petrukovich et al. 2007). Such intense ion-scale

current sheets are maintained by the stress balance between the enhanced electron anisotropy and agyrotropic ions (Artemyev et al. 2017). Current sheet thinning, therefore, occurs on a macroscopic spatial scale of several to tens of R_E (hundreds of d_i) along the tail axis, while being dominated by kinetic processes that also require the inclusion of multicomponent ion and electron distributions including low-energy plasma from the ionosphere (Runov et al. 2021).

The magnetotail reconnection region, however, is expected to be localized in the dawn-dusk direction based on the few R_E dawn-dusk extent of BBFs (Nakamura et al. 2004). THEMIS observations during a current sheet thinning support this view as the pressure gradient during the thinning was observed to increase both in the dawn-dusk direction and along the tail axis, suggesting that the thinning may take place in a localized manner (Artemyev et al. 2019).

The current sheet configuration can also be modified by the local magnetic flux transport such as dipolarization flux bundles. Nakamura et al. (2021) showed from the conjugate MMS-Cluster event (Fig. 15), where a dipolarization front developed by the fast flow is followed by a thin current sheet configuration at the wake of the flow activity, consistent with the simulation of localized fast flows/BBFs (Birn et al. 2004; Merkin et al. 2019). The localized stretched current sheet facilitates the triggering of reconnection, as predicted in the simulation of a newly formed reconnection at the wake of a dipolarization front (Sitnov et al. 2013). Statistics of the dipolarization fronts and BBFs (e.g., Dubyagin et al. 2011; Richard et al. 2022; Schmid et al. 2011) showed a dawn-dusk asymmetry in the event occurrence, skewed toward the dusk side. This represents an asymmetry in the current sheet along the dawn-dusk direction. Another possible creation of the dawn-dusk inhomogeneity of the current sheet is the flapping waves, although so far the reported flapping modes are rather consequence of reconnection (see Sect. 5.3) than the mechanism of the localized current sheet thinning.

Still there are also observations of a thin current sheet with half-thickness of one ion-gyroradius scale by Cluster (Baumjohann et al. 2007). Wang et al. (2018) reported MMS observations of an even thinner quiet current sheet with a half-thickness of $9 d_e$ without any reconnection signatures. The current sheet was bifurcated and tilted with the stability criteria of a linear tearing mode satisfied. How the onset condition is fulfilled by what processes for triggering reconnection is yet to be studied by more comprehensive multi-scale observations of the current sheet.

5.3 Multi-Scale Aspects of the Nightside Reconnection Region

Observation of magnetotail reconnection event. Due to the tailward motion of the X-line with a typical speed of a few hundreds km/s obtained from multi-point observations (Alexandrova et al. 2015; Eastwood 2005), at times together with the up-down motion of the current sheet (flapping), an X-line crossing in the magnetotail is often observed as a reversal from tailward to earthward ion flow. Figure 16 shows two examples of X-line crossing observations (A, B) with illustration of the spacecraft motion relative to the X-line (C) and the current sheet flapping (D). While the MMS observations of reconnection EDRs usually lasted only about a few seconds, the large-scale ion flow reversal from tailward to earthward takes several minutes to several tens of minutes as indicated by Fig. 16(A, B). Assuming a constant speed of the X line of few hundred km/s, the overall size of the active current-sheet region can extend up to several tens of R_E scales.

The two examples shown in Fig. 16 are from magnetotail reconnection on 11 Jul 2017 (A) when a 2-D laminar EDR (e.g., Torbert et al. 2018) was detected, and from turbulent

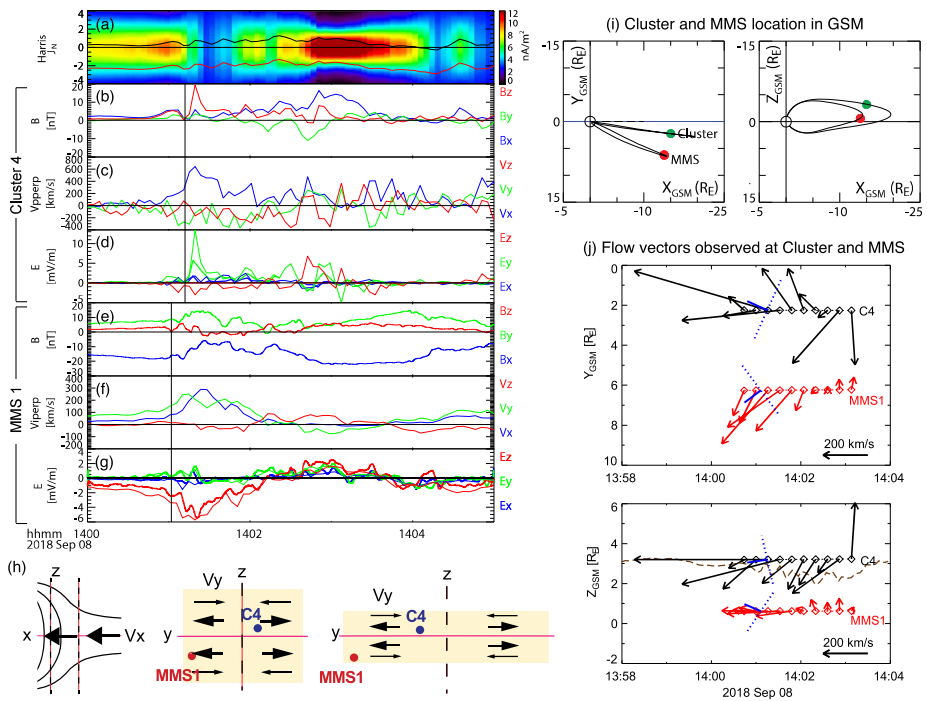


Fig. 15 Adopted from Nakamura et al. (2021). (a) The modeled current density based on conjugate MMS-Cluster observations with location of MMS and Cluster relative to the current sheet center denoted in red and black, respectively. (b-g) The magnetic flux transport associated with a dipolarization front and BBFs, behind which a thin current sheet forms facilitating the onset of reconnection (bottom illustration in panel h). (i) Location of MMS and Cluster in GSM X-Y and X-Z plane with model field lines. (j) Temporal changes of flow vectors from C4 (black) and MMS1 (red) and dipolarization front (blue) in the X-Y plane and in the X-Z plane

reconnection (B) on 26 Jul 2017 (e.g., Ergun et al. 2018) showing significant particle acceleration (for more discussion, see Oka et al. 2023, this collection). The thin current sheet region between the tailward and earthward ion flows contains complex 3-D structures for both events.

2-D and 3-D structuring inside the thin current sheet. Even for the 11 Jul 2017 event when the local EDR contains 2-D laminar reconnection features, multiple flux ropes that are characterized by localized magnetic-field strength enhancements and bipolar B_z are observed at times indicated by black arrows in Fig. 16A(d). They are ion-scale flux rope with varying axial directions, i.e., 13–55° away from the out-of-reconnection-plane direction and two of them are mostly tilted toward the direction of the reconnecting magnetic field (Teh et al. 2018). The tilted angles agree reasonably well with the predicted angles for secondary tearing modes, suggesting that these ion-scale flux ropes are likely generated by secondary tearing instabilities as those found in 3-D kinetic simulations of turbulent magnetic reconnection (e.g., Daughton et al. 2011). Stawarz et al. (2018) reported an intense, localized electric field within one of the flux ropes associated with an electron-scale vortex. Hence even though the vicinity of EDR can be explained as 2-D reconnection, the thin current sheet contained multiple small-scale 3-D magnetic structures.

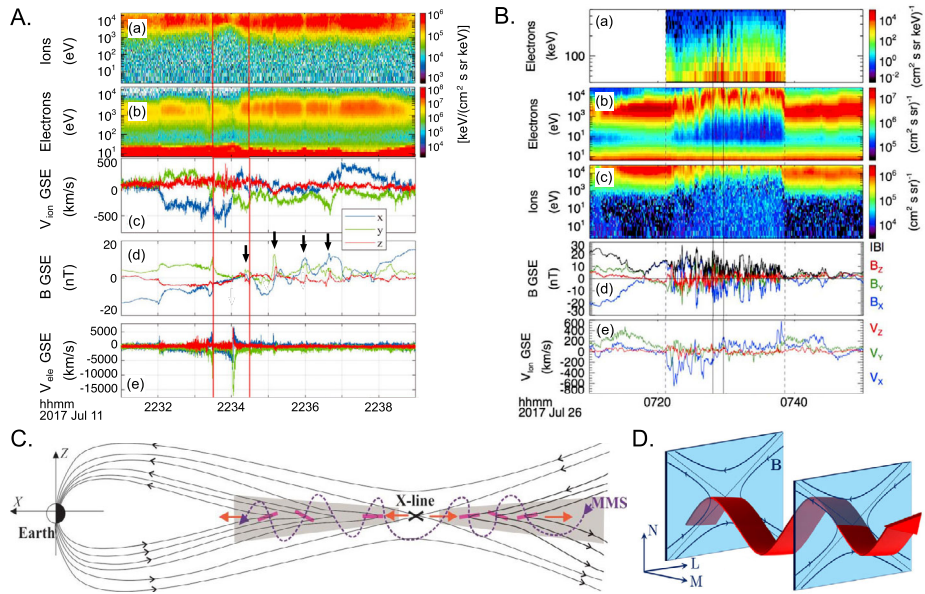


Fig. 16 Adapted from Hasegawa et al. (2019), Ergun et al. (2018), Leonenko et al. (2021), and Cozzani et al. (2021) for panels A, B, C, and D, respectively. Comparison of two MMS observations of a laminar 2-D EDR (A) and a turbulent EDR (B) with illustration of the spacecraft trajectory relative to the X-line (C) and the current sheet flapping (D)

In the prolonged disturbed thin current sheet interval shown in Fig. 16B, on the other hand, turbulent dissipation and particle acceleration are associated with strong magnetic field fluctuations (Figure 16Bd) and large-amplitude electric fields with scale-dependent energy conversion features (Ergun et al. 2018). Turbulent electric fields including significant E_{\parallel} were found to play a central role in accelerating electrons to >100 keV energies. Interesting to note is that even in this turbulent current sheet, the embedded EDR region shows a laminar profile similar to the 11 Jul 2017 event (Ergun et al. 2022). This indicates that the difference in the large-scale consequence such as particle acceleration are rather determined by the ambient parameter of the current sheet.

Effect of flapping in reconnection current sheet and beyond. Flapping kink-like motion of the current sheet is often observed in the magnetotail (Sergeev et al. 2004) associated with the active plasma sheet with fast flows (Sergeev et al. 2006). These oscillations can have frequencies ranging from a fraction of seconds to minutes and can appear on various scales. The current sheet flapping was seen in both reconnection events in Fig. 16 as an oscillating B_X (tail-aligned) component.

Small-scale separation among the four MMS spacecraft enabled the study of flapping in a thinner current sheet than previously reported. Leonenko et al. (2021) reported multiple crossings of an embedded thin current sheet with half-thickness of about few electron gyroradii or less during a prolonged interval involving a flow reversal. Resultant motion of the spacecraft relative to the thin current sheet is given in Fig. 16C. The X-line motion as well as the flapping allows for monitoring spatial/temporal changes of the current sheet. During the same event as reported by Leonenko et al. (2021), Wang et al. (2018) observed a corrugated current sheet with its normal mostly along Y_{GSM} in the flapping current sheet and showed that such current sheet corrugation enhances mixing of demagnetized ions.

The wave-like flapping structure usually propagates along the current direction as illustrated in Fig. 16D. Cozzani et al. (2021) found a flapping oscillation of > 1 Hz, near the lower hybrid drift frequency observed inside the EDR. This suggests the importance of current sheet drift instabilities in the electron-scale current sheets. Wei et al. (2019) reported a flapping motion with period of ~ 6 seconds within the ion-scale current sheet in the diffusion region that is modulated with the reconnection electric field. They concluded that the flapping motion was likely to be triggered by the periodical unsteady magnetic reconnection. PIC simulation studies (Fujimoto and Sydora 2017) showed that velocity shears of Y -directional electron and ion flows along the current sheet normal (Z) direction in the electron current layer generate the current sheet shear instability. This instability can lead to current sheet flapping with a macroscopic-scale ($\sim R_E$) wavelength (Fujimoto 2016).

Ion-scale current sheet flapping was also observed outside of the diffusion region associated with fast flows at the duskside plasma sheet (Richard et al. 2021). Drift-kink instabilities, caused by the relative drift between ions and electrons, were responsible for the flapping with a 25-second period and a phase velocity comparable to the ion duskward flow. Current sheet flapping, therefore, plays an important role in the evolution and structuring of the thin current sheet along the dawn-dusk direction in the magnetotail both inside and outside the diffusion region.

Evolution of the separatrix region of reconnection. Reconnection drives accelerated plasma beams, which spread along the magnetic field lines leading to energy-dependent dispersed structures called TDS (time-dispersed-structure) originally found in the ion beams (Sauvaud et al. 1999). Injected particles drift also perpendicular to the magnetic field due to $\mathbf{E} \times \mathbf{B}$ velocity, usually toward the plasma sheet center. Since slower particles take longer time to reach the spacecraft, this motion leads a spatial (latitudinal) dispersion due to a velocity filter effect.

The top two panels of Fig. 17A present an example of parallel electrons and ion components showing the high-energy ($>$ a few keV) beams from the reconnection region (highlighted in orange box; Wellenzohn et al. 2021). The energy-dispersed plasma beam in the separatrix region enables remote sensing of the reconnection region, assuming that the injection site along the field line is in the vicinity of the diffusion region. The high-time resolution MMS data enabled, for the first time, applying this method also to the electron data. Figure 17B shows the inverse velocity ($1/V$) spectra for electrons (upper) and ions (lower), from which the injection time and location were determined (Varsani et al. 2017). Electron and ion TDS inferred the X-line location to be 16–18 R_E downtail, which was rather close to Earth due to the strong storm-time substorm interval. Yet this location was consistent with the estimated values from a conjugate DMSP low-altitude observation of energy dispersed ions and electrons (illustrated in Fig. 17C).

Wellenzohn et al. (2021) also determined the separatrix boundary motion independent from the plasma convection so that the effect of such drift was considered in determining the location of the injection point: the reconnection region was estimated to be located at $X = (-23 \pm 1.9) R_E$ from electrons, comparable to that from ions, $X = (-24.5 \pm 0.7) R_E$. Interestingly for both events the electron injection time precedes that of the ions for several seconds, which may suggest different acceleration time scales between ions and electrons.

From the speed of the separatrix boundary relative to the convection, the reconnection electric field can be determined (Nakamura et al. 2018) [see more details in Hasegawa et al. 2023]. Wellenzohn et al. (2021) examined different signatures propagated from the reconnection site at the separatrix and used these signatures to determine the reconnection electric field. By obtaining the separatrix motion using the electron injection time, start of the electron TDS, and $E_{||}$ waves (Figure 17Ae), the reconnection electric field was estimated to be

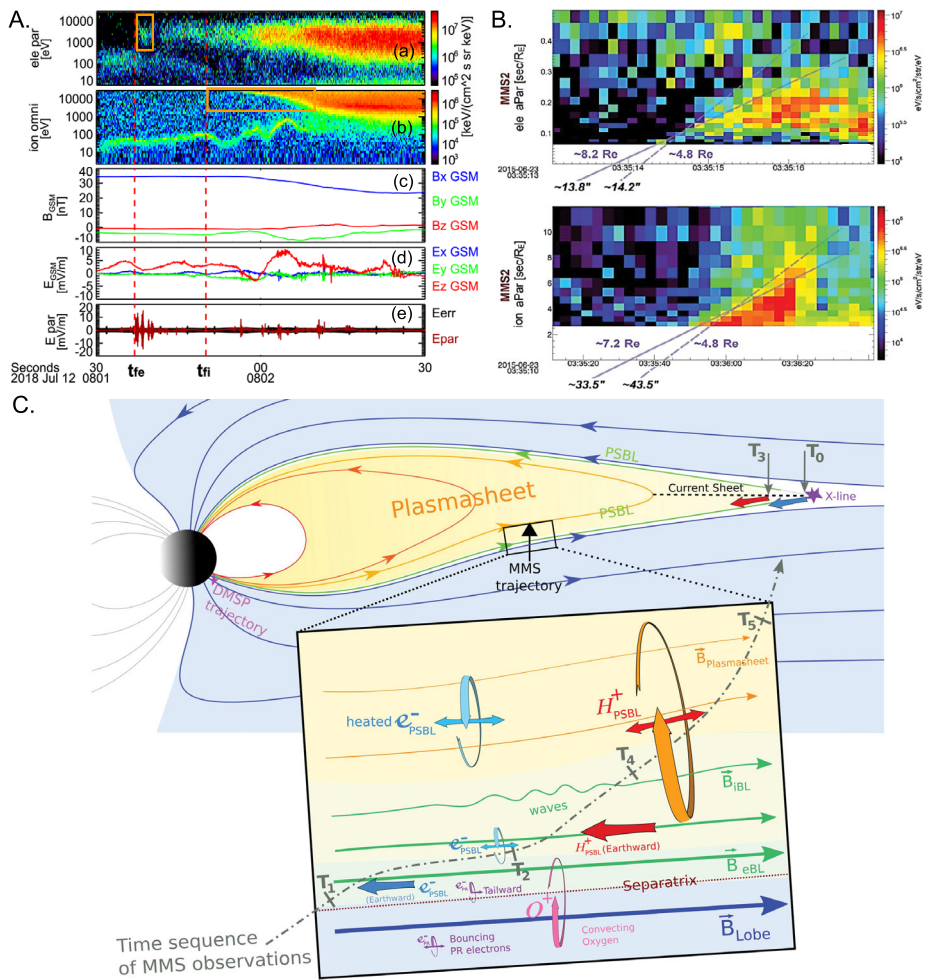


Fig. 17 Adapted from Wellenzohn et al. (2021) and Varsani et al. (2017). A. Energy-dependent time-dispersed structures (TDS) observed for electrons (a) and ions (b) and associated Hall field signatures (c, d) with parallel electric field signatures (e). B. Inverse velocity (1/V) spectra for electrons (upper) and ions (lower) from which the injection time and location can be determined. C. Diagram of TDS and velocity filter effect occurring along/around the PSBL

$E_r = 1.6\text{--}2.4$ mV/m. These values are comparable to the observed value of the 11 Jul 2017 EDR event (Fig. 16A), i.e., $E_r = 2\text{--}3$ mV/m (e.g., Genestreti et al. 2018).

Sergeev et al. (2021) showed similar patterns to Fig. 17A(b-d), i.e., dispersed ions and associated Hall-field disturbance, and cold ion beams during 9 plasma sheet boundary layer (PSBL) crossings by MMS located at distant ($>100 d_i$) and mid-distance regions ($<30\text{--}50 d_i$) from the X line. The estimated reconnection electric field from the separatrix motion using ion TDS was $E_r = 1\text{--}8$ mV/m. While these remote sensing observations require certain assumptions such as a constant speed of disturbance propagation, these studies confirm the large-scale extent of the region influenced by active reconnection and that

these remote signatures can be an alternative method to infer the temporal/spatial changes of magnetotail reconnection.

Wave-particle interaction is an important process in the separatrix region. Instabilities can develop due to the velocity shear created between the inflowing and outflowing beam (see details in Stawarz et al., this collection). High-time resolution measurements from MMS enabled to study the acceleration/heating processes. Norgren et al. (2020) reported an acceleration channel of the cold lobe electrons up to several keV at the separatrix region inside a density cavity and found that this field-aligned beam leads to electrostatic waves that thermalize the cold electron beams. The observed separatrix is adjacent to the ion outflow and hence away from the thin current sheet, being therefore a remote signature of the reconnection.

5.4 Transient Structures in the Exhaust Region

The consequences of magnetotail reconnection are manifested by geomagnetic storms and substorms on global scales (Fuselier et al., this collection), formation of flux ropes via multiple X-lines on micro-, meso-, or macroscopic scales, and generation of ion-scale dipolarization fronts formed between entrained reconnection jets and the ambient plasma (Oka et al., this collection). The second and third phenomena are frequently observed in the exhaust region of Earth's nightside reconnection. The detailed MMS data allowed resolving down-to-electron-scale structures embedded in such flux ropes and dipolarization fronts as well as interactions between flux ropes or with the ambient geomagnetic field (similar to Fig. 8f).

Electron-scale substructures were suggested to exist within the ion-scale dipolarization front and to play an important role in the energy conversion (Angelopoulos et al. 2013). The MMS measurements have revealed electron-scale density gradients, jets/currents, and electric fields, indicating electron-scale energy conversion, within both the earthward and tailward dipolarization front layer (Liu et al. 2018a; Xu et al. 2021). The dipolarization front is often subject to the ballooning/interchange instability and/or the lower hybrid drift instability (Divin et al. 2015; Hwang et al. 2011; Nakamura et al. 2016; Pan et al. 2018), suggesting the energy conversion via subsequent instabilities. Ongoing reconnection occurring at the leading edge of the dipolarization front was also identified by MMS (Marshall et al. 2020).

Sun et al. (2019) reported two types of ion-scale flux ropes, quasi 1-D and quasi 2-D structures. The former showed higher pressure inside the flux rope and the latter contained larger magnetic flux, possibly representing a later stage of the flux rope evolution. This is consistent with the theoretical expectation that the quasi 2-D structure is in a lower energy state.

Re-reconnection between an earthward propagating flux rope and Earth's dipole magnetic fields was reported by Man et al. (2018). Furthermore, Poh et al. (2019) further investigated the ionospheric response to such interaction using the magnetic field perturbations observed by ground magnetometers. Conjugate ionospheric observations at the ionospheric footprint of the re-reconnection site showed enhanced horizontal currents as observed by AMPERE and increased ionospheric convection by superDARN. This implies the large-scale impacts of the transient structures and their interactions with background fields and pre-existing plasmas occurring in the exhaust region of magnetotail reconnection.

6 Key Aspects with Relevance and Applications to Other Plasma Systems

In this paper we reviewed multi-scale aspects of magnetic reconnection beyond the diffusion region and the global-scale magnetospheric dynamics as described by the Dungey Cycle. Recent high time-resolution in-situ observations and state-of-the-art numerical techniques have significantly advanced our understanding of cross-scale reconnection processes. Table 1 presents the key features of these advancements, focusing on the dominant scales identified for each process. These findings are categorized according to various terrestrial regions, characterized by different magnetic topologies and physical parameters across the current sheet. The results from these studies can be applied to other regimes encompassing solar plasmas, planetary magnetospheres, and other heliospheric and astrophysical systems. We also acknowledge the unsolved problems, which can serve as guidance for future studies on magnetic reconnection in geospace, as well as throughout the heliosphere and the universe.

Acknowledgements The authors thank the International Space Science Institute (ISSI) for hosting the team and relevant meetings. K.-J.H., S.F. and K.D. were supported by NASA's MMS project at SwRI. K.-J.H and K.D. were supported by NASA 80NSSC23K0417 and 80NSSC18K1337. J.E. and H.H were supported by UKRI/STFC ST/W001071/1 and JSPS Grant-in-aid for Scientific Research KAKENHI 21K03504, respectively.

Table 1 Notable findings on multi-scale aspects of reconnection, applications to other systems, and unsolved problems

Location	Key features	Applications to other systems	Unsolved problems
Reconnection at the fore-shock, shock, and down-stream magneto-sheath	<p><i>Electron scale:</i></p> <ul style="list-style-type: none"> • Electron-only reconnection with or without a guide field in the foreshock, the shock transition region, and the downstream magnetosheath • The prevalent occurrence of electron-only reconnection, possibly in association with turbulent systems <p><i>Ion scale:</i></p> <ul style="list-style-type: none"> • Ion-scale young current sheets exhibiting electron jets only • Cyclical reformation of the shock front leading to the formation of the current sheet • Ion-scale flux ropes in the foreshock <p><i>MHD scale:</i></p> <ul style="list-style-type: none"> • 40% of shock crossings contain reconnecting current sheets. • The occurrence rate is strongly or weakly biased toward the quasi-parallel shock at the bow shock and the magnetosheath. • Large-scale discontinuities interacting with the bow shock compress a current sheet, triggering reconnection. • Current sheets initiated at the bow shock continue to influence energy processing downstream 	<ul style="list-style-type: none"> • Planetary magneto-spheres with the bow shock and the shocked solar wind region • The coupled system of the shock, reconnection, and turbulence in the universe 	<ul style="list-style-type: none"> • Whether or not electron-only reconnection is a temporal evolution to ion reconnection • Detailed behavior of the magnetosheath (reconnection and turbulence features) downstream of different bow shock magnetic geometries • Pathway and impacts of fluctuations initiated at the foreshock/shock through the magnetosheath to the magnetopause

Table 1 (Continued)

Location	Key features	Applications to other systems	Unsolved problems
Dayside magneto-pause reconnection	<p><i>Electron scale:</i></p> <ul style="list-style-type: none"> • Dayside electron diffusion region (EDR) characterized by a perpendicular crescent of electron distribution functions and positive Ohmic energy exchange • Outer EDR characterized by parallel crescents and negative Ohmic energy exchange, with Hall electron flows leading to magnetic pileup affecting the opening angle (reconnection rate). • Electron vortex and phase space holes along the magnetospheric separatrix • EDR detected at the interface of interacting flux ropes or interlinked flux tubes <p><i>Ion scale:</i></p> <ul style="list-style-type: none"> • Density asymmetry across the current sheet, leading to the displacement of the flow stagnant point from the X-line, symmetric Hall electric field, and bipolar Hall magnetic field • Multiple ion components implying the location of the X-line and magnetic field topologies • Formation of ion-scale secondary islands/flux ropes/flux transfer events (FTEs) • Coalescence or interaction of secondary islands/flux ropes <p><i>MHD scale:</i></p> <ul style="list-style-type: none"> • The extent and orientation of X-lines depend on background magnetic field topologies and a guide field. • Time-varying upstream conditions lead to the formation of secondary X-lines to adjust the orientation. • Generation of interlinked flux tubes that evolve their magnetic connectivity via localized reconnection • Magnetosphere-ionosphere coupling processes caused by unsteady dayside reconnection or FTEs 	<ul style="list-style-type: none"> • Planetary magneto-spheres with the dayside magnetopause across which magnetic shear and density gradient co-exist • Solar/helio-spheric/astro-physical current sheets undergoing asymmetric reconnection with a guide field 	<ul style="list-style-type: none"> • Detailed 3-D topology including the orientation of the X-line(s) with controlling parameters • Mechanisms determining the generation of primary and secondary X-lines and resultant reconnection rates • Evolution and fate of various types of flux ropes/flux transfer events generated on the dayside magnetopause via multiple X-lines

Funding Open access funding provided by Österreichische Akademie der Wissenschaften.

Declarations

Competing Interests All the authors declare that the work was conducted without any commercial or financial relationships that could be construed as potential conflicts of interest.

Open Access This article is licensed under a Creative Commons Attribution 4.0 International License, which permits use, sharing, adaptation, distribution and reproduction in any medium or format, as long as you give appropriate credit to the original author(s) and the source, provide a link to the Creative Commons licence, and indicate if changes were made. The images or other third party material in this article are included in the article's Creative Commons licence, unless indicated otherwise in a credit line to the material. If material is

Table 1 (Continued)

Location	Key features	Applications to other systems	Unsolved problems
Flankside magneto-pause reconnection	<p><i>Electron scale:</i></p> <ul style="list-style-type: none"> • Current sheet thinning to electron scales via a velocity shear leading to Vortex-Induced Reconnection (Type-I VIR) • Highly swirled field lines via the flow vortex leading to secondary reconnection (Type-II VIR) • In-situ observations of EDR during VIR <p><i>Ion scale:</i></p> <ul style="list-style-type: none"> • X-line drift due to the upstream magnetosheath flow • Asymmetric exhaust region due to the combined effects of density gradient and velocity shear across the current sheet • Formation of ion-scale flux ropes along the Kelvin-Helmholtz (KH) vortex boundary <p><i>MHD scale:</i></p> <ul style="list-style-type: none"> • In-situ evidence for mid-latitude reconnection that occurs due to a 3-D twist of magnetospheric and magnetosheath fields induced by KH vortices • The latitudinal extent of both in-plane (VIR) and mid-latitude reconnection that becomes wider with nonlinear KH instability evolution • VIR-driven turbulence forming a mixing boundary layer and large-scale mass transport beyond the boundary layer toward the central magnetosphere 	<ul style="list-style-type: none"> • Planetary magneto-spheres with the flankside magnetopause across which density gradient and velocity shear co-exist • Solar/helio-spheric/astro-physical current sheets undergoing asymmetric reconnection with a velocity shear 	<ul style="list-style-type: none"> • The combined effects of density asymmetry, velocity shear, and a guide field (parametric study) • In-plane (VIR) and out-of-plane (mid-latitude) reconnection with their combined effect on the solar wind transport • The propagation of flankside VIR-driven fluctuations and their impact on the central plasma sheet behavior
Magnetotail reconnection	<p><i>Electron scale:</i></p> <ul style="list-style-type: none"> • Nightside EDR characterized by multiple (perpendicular) crescents, positive Ohmic energy exchange, and large electron vorticity • Laminar EDR detected during both 2-D laminar and turbulent reconnection • EDR detected at the interface of interacting flux ropes or at the leading edge of a flux rope (re-reconnection) • Electron-scale structures embedded within the dipolarization front <p><i>Ion scale:</i></p> <ul style="list-style-type: none"> • Existence of multiple ion scales in association with cold and/or heavy ion components • Ion-scale flapping current sheet enhancing the mixing of demagnetized ions • Transient structures shown in the exhaust region, such as ion-scale flux ropes and both earthward and tailward dipolarization fronts 	<ul style="list-style-type: none"> • Planetary magneto-spheres with the nightside current sheet along which plasma and magnetic field gradients co-exist • Solar/helio-spheric/astro-physical current sheets undergoing symmetric reconnection 	<ul style="list-style-type: none"> • Onset mechanism of the triggering of reconnection in a marginally stable magnetotail current sheet • Local or ambient parameters determining the consequences of reconnection (e.g., reconnection rate) • Causality between reconnection and current sheet flapping

Table 1 (Continued)

Location	Key features	Applications to other systems	Unsolved problems
	<p><i>MHD scale:</i></p> <ul style="list-style-type: none"> ● Dawn-dusk extent of the magnetotail X-line implied by BBFs ● Current sheet thinning after an earthward-moving dipolarization front, triggering reconnection ● Current sheet flapping with low to high frequency (similar to lower-hybrid frequency) ● Remote sensing of tail reconnection location using both electron and ion dispersion signatures ● Re-reconnection influencing the high-latitude ionospheric currents 		

not included in the article's Creative Commons licence and your intended use is not permitted by statutory regulation or exceeds the permitted use, you will need to obtain permission directly from the copyright holder. To view a copy of this licence, visit <http://creativecommons.org/licenses/by/4.0/>.

References

- Ahmadi N, Eriksson S, Newman D, Andersson L, Ergun RE et al (2022) J Geophys Res Space Phys 127(8):1–12. <https://doi.org/10.1029/2022JA030702>
- Akhavan-Tafti M, Palmroth M, Slavin JA, Battarbee M, Ganse U et al (2020) J Geophys Res Space Phys 125(7):e2019JA027410. <https://doi.org/10.1029/2019JA027410>
- Alexandrova A, Nakamura R, Semenov VS, Nakamura TKM (2015) Geophys Res Lett 42(12):4685–4693. <https://doi.org/10.1002/2015GL064421>
- Angelopoulos V, Baumjohann W, Kennel CF, Coroniti FV, Kivelson MG et al (1992) J Geophys Res 97(A4):4027. <https://doi.org/10.1029/91JA02701>
- Angelopoulos V, Runov A, Zhou XZ, Turner DL, Kiehas SA et al (2013) Science 341(6153):1478–1482. <https://doi.org/10.1126/science.1236992>
- Archer MO, Turner DL, Eastwood JP, Schwartz SJ, Horbury TS (2015) Planet Space Sci 106:56–66. <https://doi.org/10.1016/j.pss.2014.11.026>
- Artemyev AV, Angelopoulos V, Runov A, Petrokovich AA (2016) J Geophys Res Space Phys. <https://doi.org/10.1002/2016JA022779>
- Artemyev AV, Angelopoulos V, Liu J, Runov A (2017) Geophys Res Lett. <https://doi.org/10.1002/2016GL072011>
- Artemyev AV, Angelopoulos V, Runov A, Petrukovich AA (2019) J Geophys Res Space Phys 124(1):264–278. <https://doi.org/10.1029/2018JA026113>
- Artemyev A, Lu S, El-Alaoui M, Lin Y, Angelopoulos V et al (2021) Geophys Res Lett 48(6):1–9. <https://doi.org/10.1029/2020GL092153>
- Bai SC, Shi Q, Liu TZ, Zhang H, Yue C et al (2020) Geophys Res Lett 47(5):1–9. <https://doi.org/10.1029/2019GL085933>
- Balogh A, Treumann RA (2013) Physics of collisionless shocks. ISSI scientific report series, vol 12. Springer, New York. <https://doi.org/10.1007/978-1-4614-6099-2>
- Baumjohann W, Roux A, Le Contel O, Nakamura R, Birn J et al (2007) Ann Geophys 25(6):1365–1389. <https://doi.org/10.5194/angeo-25-1365-2007>
- Berchem J, Russell CT (1982) J Geophys Res 87(A4):2108. <https://doi.org/10.1029/JA087iA04p02108>
- Bessho N, Chen L-J, Wang S, Hesse M, Wilson LB (2019) Geophys Res Lett 46(16):9352–9361. <https://doi.org/10.1029/2019GL083397>
- Bessho N, Chen L-J, Wang S, Hesse M, Wilson LB et al (2020) Phys Plasmas 27(9):092901. <https://doi.org/10.1063/5.0012443>
- Bessho N, Chen L-J, Stawarz JE, Wang S, Hesse M et al (2022) Phys Plasmas 29(4):042304. <https://doi.org/10.1063/5.0077529>

- Birn J, Schindler K (2002) *J Geophys Res* 107(A7):1117. <https://doi.org/10.1029/2001JA000291>
- Birn J, Raeder J, Wang YL, Wolf RA, Hesse M (2004) *Ann Geophys.* <https://doi.org/10.5194/angeo-22-1773-2004>
- Bohdan A, Pohl M, Niemiec J, Vafin S, Matsumoto Y et al (2020) *Astrophys J* 893(1):6. <https://doi.org/10.3847/1538-4357/ab7cd6>
- Borgogno D, Califano F, Faganello M, Pegoraro F (2015) *Phys Plasmas.* <https://doi.org/10.1063/1.4913578>
- Burch JL, Reiff PH, Heelis RA, Winningham JD, Hanson WB et al (1982) *Geophys Res Lett* 9(9):921–924. <https://doi.org/10.1029/GL009i009p00921>
- Burch JL, Torbert RB, Phan TD, Chen LJ, Moore TE et al (2016) *Science* 352(6290):aaf2939. <https://doi.org/10.1126/science.aaf2939>
- Cassak PA, Otto A (2011) *Phys Plasmas* 18(7):074501. <https://doi.org/10.1063/1.3609771>
- Chandrasekhar S (1961) Oxford University Press, London
- Chang C, Huang K, Lu Q, Sang L, Lu S et al (2021) *J Geophys Res Space Phys* 126(7):1–11. <https://doi.org/10.1029/2021JA029290>
- Chen XL, Morrison PJ (1990) *Phys Fluids, B Plasma Phys* 2(3):495–507. <https://doi.org/10.1063/1.859339>
- Chen LJ, Hesse M, Wang S, Bessho N, Daughton W (2016) *Geophys Res Lett* 43(6):2405–2412. <https://doi.org/10.1002/2016GL068243>
- Chen ZZ, Fu HS, Wang Z, Liu CM, Xu Y (2019) *Geophys Res Lett* 46(17–18):10209–10218. <https://doi.org/10.1029/2019GL084360>
- Cozzani G, Khotyaintsev YV, Graham DB, Egedal J, André M et al (2021) *Phys Rev Lett* 127(21):1–8. <https://doi.org/10.1103/PhysRevLett.127.215101>
- Daughton W, Roytershteyn V, Karimabadi H, Yin L, Albright BJ et al (2011) *Nat Phys* 7(7):539–542. <https://doi.org/10.1038/nphys1965>
- Denton RE, Torbert RB, Hasegawa H, Dors I, Genestreti KJ et al (2020) *J Geophys Res Space Phys* 125(2):1–28. <https://doi.org/10.1029/2019ja027481>
- Divin A, Khotyaintsev YV, Vaivads A, André M (2015) *J Geophys Res Space Phys* 120(2):1124–1132. <https://doi.org/10.1002/2014JA020528>
- Doss CE, Komar CM, Cassak PA, Wilder FD, Eriksson S et al (2015) *J Geophys Res Space Phys* 120(9):7748–7763. <https://doi.org/10.1002/2015JA021489>
- Dubyagin S, Sergeev V, Apatenkov S, Angelopoulos V, Runov A et al (2011) *Geophys Res Lett* 38(8):L08102. <https://doi.org/10.1029/2011GL047016>
- Dunlop MW, Zhang QH, Bogdanova YV, Trattner KJ, Pu Z et al (2011) *Ann Geophys* 29(9):1693–1697. <https://doi.org/10.5194/angeo-29-1683-2011>
- Eastwood JP (2005) *Geophys Res Lett* 32(11):L11105. <https://doi.org/10.1029/2005GL022509>
- Eastwood JP, Mistry R, Phan TD, Schwartz SJ, Ergun RE et al (2018) *Geophys Res Lett.* <https://doi.org/10.1029/2018GL077670>
- Egedal J, Fox W, Katz N, Porkolab M, Øieroset M et al (2008) *J Geophys Res Space Phys* 113:A12207. <https://doi.org/10.1029/2008JA013520>
- Ergun RE, Goodrich KA, Wilder FD, Ahmadi N, Holmes JC et al (2018) *Geophys Res Lett.* <https://doi.org/10.1002/2018GL076993>
- Ergun RE, Pathak N, Usanova ME, Qi Y, Vo T et al (2022) *Astrophys J Lett* 935(1):L8. <https://doi.org/10.3847/2041-8213/ac81d4>
- Eriksson S, Lavraud B, Wilder FD, Stawarz JE, Giles BL et al (2016) *Geophys Res Lett* 43(11):5606–5615. <https://doi.org/10.1002/2016GL068783>
- Fadanelli S, Faganello M, Califano F, Cerri SS, Pegoraro F et al (2018) *J Geophys Res Space Phys* 123(11):9340–9356. <https://doi.org/10.1029/2018JA025626>
- Faganello M, Califano F (2017) *J Plasma Phys* 83(6):535830601. <https://doi.org/10.1017/S0022377817000770>
- Faganello M, Califano F, Pegoraro F (2008) *Phys Rev Lett* 101(10):105001. <https://doi.org/10.1103/PhysRevLett.101.105001>
- Faganello M, Califano F, Pegoraro F, Andreussi T (2012) *Europhys Lett* 100(6):69001. <https://doi.org/10.1209/0295-5075/100/69001>
- Faganello M, Sisti M, Califano F, Lavraud B (2022) *Plasma Phys Control Fusion* 64(4):044014. <https://doi.org/10.1088/1361-6587/ac43f0>
- Fargette N, Lavraud B, Øieroset M, Phan TD, Toledo-Redondo S et al (2020) *Geophys Res Lett* 47(6):1–9. <https://doi.org/10.1029/2019GL086726>
- Fermo R, Drake J, Swisdak M (2012) *Phys Rev Lett* 108(25):255005. <https://doi.org/10.1103/PhysRevLett.108.255005>
- Fu HS, Vaivads A, Khotyaintsev YV, Olshevsky V, André M et al (2015) *J Geophys Res Space Phys.* <https://doi.org/10.1002/2015JA021082>
- Fujimoto K (2016) *Geophys Res Lett* 43(20):10557–10564. <https://doi.org/10.1002/2016GL078010>

- Fujimoto K, Sydora RD (2017) *J Geophys Res Space Phys* 122(5):5418–5430. <https://doi.org/10.1002/2017JA024079>
- Fuselier SA (2002) *J Geophys Res* 107(A7):1111. <https://doi.org/10.1029/2001JA900165>
- Fuselier SA, Trattner KJ, Petrinec SM, Denton MH, Toledo-Redondo S et al (2019a) *Geophys Res Lett* 46(12):6204–6213. <https://doi.org/10.1029/2019GL082384>
- Fuselier SA, Trattner KJ, Petrinec SM, Pritchard KR, Burch JL et al (2019b) *J Geophys Res Space Phys* 124(11):8524–8534. <https://doi.org/10.1029/2019JA027143>
- Fuselier SA, Webster JM, Trattner KJ, Petrinec SM, Genestreti KJ et al (2021) *J Geophys Res Space Phys* 126(12):1–16. <https://doi.org/10.1029/2021JA029789>
- Genestreti KJ, Nakamura TKM, Nakamura R, Denton RE, Torbert RB et al (2018) *J Geophys Res Space Phys* 123(11):9130–9149. <https://doi.org/10.1029/2018JA025711>
- Genestreti KJ, Liu Y-H, Phan T-D, Denton RE, Torbert RB et al (2020) *J Geophys Res Space Phys* 125(10):1–16. <https://doi.org/10.1029/2020JA027985>
- Gingell I, Schwartz SJ, Eastwood JP, Burch JL, Ergun RE et al (2019) *Geophys Res Lett* 46(3):1177–1184. <https://doi.org/10.1029/2018GL081804>
- Gingell I, Schwartz SJ, Eastwood JP, Stawarz JE, Burch JL et al (2020) *J Geophys Res Space Phys* 125(1):e2019JA027119. <https://doi.org/10.1029/2019JA027119>
- Gingell I, Schwartz SJ, Kucharek H, Farrugia CJ, Trattner KJ (2021) *Phys Plasmas* 28(10):102902. <https://doi.org/10.1063/5.0062520>
- Gosling JT (2012) *Space Sci Rev* 172(1–4):187–200. <https://doi.org/10.1007/s11214-011-9747-2>
- Graham DB, Khotyaintsev YV, Norgren C, Vaivads A, André M et al (2017) *J Geophys Res Space Phys* 122(1):517–533. <https://doi.org/10.1002/2016JA023572>
- Greco A, Matthaeus WH, Perri S, Osman KT, Servidio S et al (2018) *Space Sci Rev* 214(1):1. <https://doi.org/10.1007/s11214-017-0435-8>
- Guo Z, Lin Y, Wang X (2021a) *J Geophys Res Space Phys* 126(4):1–20. <https://doi.org/10.1029/2020JA028853>
- Guo Z, Lin Y, Wang X, Du A (2021b) *J Geophys Res Space Phys* 126(12):e2021JA029979. <https://doi.org/10.1029/2021JA029979>
- Hamrin M, Gunell H, Goncharov O, De Spiegeleer A, Fuselier S et al (2019) *J Geophys Res Space Phys* 124(11):8507–8523. <https://doi.org/10.1029/2019JA027006>
- Hasegawa H, Fujimoto M, Takagi K, Saito Y, Mukai T et al (2006) *J Geophys Res* 111:A09203. <https://doi.org/10.1029/2006JA011728>
- Hasegawa H, Retinó A, Vaivads A, Khotyaintsev Y, André M et al (2009) *J Geophys Res Space Phys* 114(12):1–20. <https://doi.org/10.1029/2009JA014042>
- Hasegawa H, Zhang H, Lin Y, Sonnerup BU, Schwartz SJ et al (2012) *J Geophys Res Space Phys* 117(9):1–11. <https://doi.org/10.1029/2012JA017920>
- Hasegawa H, Kitamura N, Saito Y, Nagai T, Shinohara I et al (2016) *Geophys Res Lett* 43(10):4755–4762. <https://doi.org/10.1002/2016GL069225>
- Hasegawa H, Denton RE, Nakamura R, Genestreti KJ, Nakamura TKM et al (2019) *J Geophys Res Space Phys* 124(1):122–138. <https://doi.org/10.1029/2018JA026051>
- Hasegawa H, Nakamura TKM, Gershman DJ, Nariyuki Y, Viñas AF et al (2020) *J Geophys Res Space Phys* 125(3):1–19. <https://doi.org/10.1029/2019JA027595>
- Hasegawa H, Denton RE, Dokgo K, Hwang K-J, Nakamura TKM et al (2023) *J Geophys Res Space Phys*. <https://doi.org/10.1029/2022ja031092>
- Hesse M, Aunai N, Sibeck D, Birn J (2014) *Geophys Res Lett* 41(24):8673–8680. <https://doi.org/10.1002/2014GL061586>
- Hoilijoki S, Pucci F, Ergun RE, Schwartz SJ, Wilder FD et al (2021) *J Geophys Res Space Phys* 126(5):1–13. <https://doi.org/10.1029/2020JA029046>
- Holmes JC, Ergun RE, Nakamura R, Roberts O, Wilder FD et al (2019) *J Geophys Res Space Phys* 124(11):8788–8803. <https://doi.org/10.1029/2019JA026974>
- Hsieh MS, Otto A (2014) *J Geophys Res Space Phys* 119(5):3430–3443. <https://doi.org/10.1002/2013JA019459>
- Hwang KJ, Goldstein ML, Lee E, Pickett JS (2011) *J Geophys Res Space Phys* 116(4):1–16. <https://doi.org/10.1029/2010JA015742>
- Hwang KJ, Sibeck DG, Giles BL, Pollock CJ, Gershman D et al (2016) *Geophys Res Lett* 43(18):9434–9443. <https://doi.org/10.1002/2016GL070934>
- Hwang KJ, Sibeck DG, Choi E, Chen LJ, Ergun RE et al (2017) *Geophys Res Lett* 44(5):2049–2059. <https://doi.org/10.1002/2017GL072830>
- Hwang KJ, Sibeck DG, Burch JL, Choi E, Fear RC et al (2018) *J Geophys Res Space Phys* 123(10):8473–8488. <https://doi.org/10.1029/2018JA025611>

- Hwang KJ, Choi E, Dokgo K, Burch JL, Sibeck DG et al (2019) *Geophys Res Lett* 46(12):6287–6296. <https://doi.org/10.1029/2019GL082710>
- Hwang K-J, Dokgo K, Choi E, Burch JL, Sibeck DG et al (2020a) *J Geophys Res Space Phys* 125(4):e2019JA027665. <https://doi.org/10.1029/2019JA027665>
- Hwang KJ, Nishimura Y, Coster AJ, Gillies RG, Fear RC et al (2020b) *J Geophys Res Space Phys* 125(6):1–15. <https://doi.org/10.1029/2019JA027674>
- Hwang K-J, Burch JL, Russell CT, Choi E, Dokgo K et al (2021) *Astrophys J* 914(1):26. <https://doi.org/10.3847/1538-4357/abf8b1>
- Hwang K-J, Weygand JM, Sibeck DG, Burch JL, Goldstein ML et al (2022) *Front Astron Space Sci* 9:1–15. <https://doi.org/10.3389/fspas.2022.895514>
- Jiang K, Huang SY, Fu HS, Yuan ZG, Deng XH et al (2021) *Astrophys J* 922(1):56. <https://doi.org/10.3847/1538-4357/ac2500>
- Johnson JR, Wing S (2015) *J Geophys Res Space Phys* 120(5):3987–4008. <https://doi.org/10.1002/2014JA020312>
- Johnson JR, Wing S, Delamere P, Petrinesc S, Kavosi S (2021) *J Geophys Res Space Phys* 126(2):1–15. <https://doi.org/10.1029/2020JA028583>
- Kacem I, Jacquey C, Génot V, Lavraud B, Vernisse Y et al (2018) *J Geophys Res Space Phys* 123(3):1779–1793. <https://doi.org/10.1002/2017JA024537>
- Karimabadi H, Roytershteyn V, Vu HX, Omelchenko YA, Scudder J et al (2014) *Phys Plasmas* 21(6):062308. <https://doi.org/10.1063/1.4882875>
- Kieokaew R, Lavraud B, Foullon C, Toledo-Redondo S, Fargette N et al (2020) *J Geophys Res Space Phys* 125(6):1–18. <https://doi.org/10.1029/2019JA027527>
- Knoll DA, Chacón L (2002) *Phys Rev Lett*. <https://doi.org/10.1103/PhysRevLett.88.215003>
- Kropotina JA, Webster L, Artemyev AV, Bykov AM, Vainchtein DL et al (2021) *Astrophys J* 913(2):142. <https://doi.org/10.3847/1538-4357/abf6c7>
- La Belle-Hamer AL, Otto A, Lee LC (1995) *J Geophys Res* 100(A7):11875–11889. <https://doi.org/10.1029/94JA00969>
- Lavraud B, Zhang YC, Vernisse Y, Gershman DJ, Dorelli J et al (2016) *Geophys Res Lett* 43(7):3042–3050. <https://doi.org/10.1002/2016GL068359>
- Lee LC, Fu ZF (1985) *Geophys Res Lett* 12(2):105–108. <https://doi.org/10.1029/GL012i002p00105>
- Leonenko MV, Grigorenko EE, Zelenyi LM, Malova HV, Malykhin AY et al (2021) *J Geophys Res Space Phys* 126(11):e2021JA029641. <https://doi.org/10.1029/2021JA029641>
- Li W, Raeder J, Thomsen MF, Lavraud B (2008) *J Geophys Res Space Phys* 113(A4):A04204. <https://doi.org/10.1029/2007JA012604>
- Liu CM, Fu HS, Xu Y, Khotyaintsev YV, Burch JL et al (2018a) *Geophys Res Lett*. <https://doi.org/10.1029/2018GL077928>
- Liu YH, Hesse M, Li TC, Kuznetsova M, Le A (2018b) *J Geophys Res Space Phys* 123(6):4908–4920. <https://doi.org/10.1029/2018JA025410>
- Liu YY, Fu HS, Olshevsky V, Pontin DI, Liu CM et al (2019) *Astrophys J Suppl Ser* 244(2):31. <https://doi.org/10.3847/1538-4365/ab391a>
- Liu TZ, Lu S, Turner DL, Gingell I, Angelopoulos V et al (2020) *J Geophys Res Space Phys* 125(4):1–11. <https://doi.org/10.1029/2020JA027822>
- Lockwood M, Smith MF (1989) *Geophys Res Lett* 16(8):879–882. <https://doi.org/10.1029/GL016i008p00879>
- Lu Q, Wang H, Wang X, Lu S, Wang R et al (2020) *Geophys Res Lett* 47(1):1–6. <https://doi.org/10.1029/2019GL085661>
- Lu Q, Yang Z, Wang H, Wang R, Huang K et al (2021) *Astrophys J* 919(1):28. <https://doi.org/10.3847/1538-4357/ac18c0>
- Ma X, Otto A, Delamere PA (2014a) *J Geophys Res Space Phys* 119(2):808–820. <https://doi.org/10.1002/2013JA019225>
- Ma X, Otto A, Delamere PA (2014b) *J Geophys Res Space Phys* 119(2):781–797. <https://doi.org/10.1002/2013JA019224>
- Ma X, Delamere P, Otto A, Burkholder B (2017) *J Geophys Res Space Phys* 122(10):10,382–10,395. <https://doi.org/10.1002/2017JA024394>
- Maheshwari K, Phan TD, Øieroset M, Fargette N, Lavraud B et al (2022) *Astrophys J* 940(2):177. <https://doi.org/10.3847/1538-4357/ac9405>
- Man HY, Zhou M, Deng XH, Fu HS, Zhong ZH et al (2018) *Geophys Res Lett* 45(17):8729–8737. <https://doi.org/10.1029/2018GL079778>
- Marshall AT, Burch JL, Reiff PH, Webster JM, Torbert RB et al (2020) *J Geophys Res Space Phys* 125(1):1–9. <https://doi.org/10.1029/2019JA027296>


- Matsumoto Y, Amano T, Kato TN, Hoshino M (2015) *Science* 347(6225):974–978. <https://doi.org/10.1126/science.1260168>
- Maynard NC, Burke WJ, Ober DM, Farrugia CJ, Kucharek H et al (2007) *J Geophys Res Space Phys* 112(A12):A12219. <https://doi.org/10.1029/2007JA012293>
- Mejnertsen L, Eastwood JP, Chittenden JP (2021) *Front Astron Space Sci* 8:1–15. <https://doi.org/10.3389/fspas.2021.758312>
- Merkin VG, Panov EV, Sorathia KA, Ukhorskiy AY (2019) *J Geophys Res Space Phys* 124(11):8647–8668. <https://doi.org/10.1029/2019JA026872>
- Miura A (1984) *J Geophys Res* 89(A2):801. <https://doi.org/10.1029/JA089iA02p00801>
- Miura A, Pritchett PL (1982) *J Geophys Res*. <https://doi.org/10.1029/JA087iA09p07431>
- Nakamura TKM, Daughton W (2014) *Geophys Res Lett* 41(24):8704–8712. <https://doi.org/10.1002/2014GL061952>
- Nakamura TKM, Fujimoto M (2005) *Geophys Res Lett* 32:L21102. <https://doi.org/10.1029/2005GL023362>
- Nakamura R, Baumjohann W, Mouikis C, Kistler LM, Runov A et al (2004) *Geophys Res Lett* 31(9):L09804. <https://doi.org/10.1029/2004GL019558>
- Nakamura TKM, Fujimoto M, Otto A (2006) *Geophys Res Lett*. <https://doi.org/10.1029/2006GL026318>
- Nakamura TKM, Fujimoto M, Otto A (2008) *J Geophys Res Space Phys*. <https://doi.org/10.1029/2007JA012803>
- Nakamura TKM, Hasegawa H, Shinohara I, Fujimoto M (2011) *J Geophys Res Space Phys*. <https://doi.org/10.1029/2010JA016046>
- Nakamura TKM, Daughton W, Karimabadi H, Eriksson S (2013) *J Geophys Res Space Phys* 118(9):5742–5757. <https://doi.org/10.1002/jgra.50547>
- Nakamura R, Sergeev VA, Baumjohann W, Plaschke F, Magnes W et al (2016) *Geophys Res Lett* 43(10):4841–4849. <https://doi.org/10.1002/2016GL068768>
- Nakamura TKM, Eriksson S, Hasegawa H, Zenitani S, Li WY et al (2017a) *J Geophys Res Space Phys* 122(11):11505–11522. <https://doi.org/10.1002/2017JA024346>
- Nakamura TKM, Hasegawa H, Daughton W, Eriksson S, Li WY et al (2017b) *Nat Commun*. <https://doi.org/10.1038/s41467-017-01579-0>
- Nakamura TKM, Nakamura R, Varsani A, Genestreti KJ, Baumjohann W et al (2018) *Geophys Res Lett* 45(9):3829–3837. <https://doi.org/10.1029/2018GL078340>
- Nakamura TKM, Stawarz JE, Hasegawa H, Narita Y, Franci L et al (2020) *J Geophys Res Space Phys* 125(3):1–18. <https://doi.org/10.1029/2019JA027515>
- Nakamura R, Baumjohann W, Nakamura TKM, Panov EV, Schmid D et al (2021) *J Geophys Res Space Phys* 126(10):1–19. <https://doi.org/10.1029/2021JA029518>
- Nishino MN, Hasegawa H, Saito Y, Kitamura N, Miyashita Y et al (2022) *J Geophys Res Space Phys* 127(1):1–16. <https://doi.org/10.1029/2021JA029747>
- Norgren C, Hesse M, Graham DB, Khotyaintsev YV, Tenfjord P et al (2020) *J Geophys Res Space Phys* 125(4):e2019JA027440. <https://doi.org/10.1029/2019JA027440>
- Nykyri K, Otto A (2001) *Geophys Res Lett* 28(18):3565–3568. <https://doi.org/10.1029/2001GL013239>
- Nykyri K, Ma X, Dimmock A, Foullon C, Otto A et al (2017) *J Geophys Res Space Phys* 122(9):9489–9512. <https://doi.org/10.1002/2017JA024374>
- Øieroset M, Phan TD, Haggerty C, Shay MA, Eastwood JP et al (2016) *Geophys Res Lett* 43(11):5536–5544. <https://doi.org/10.1002/2016GL069166>
- Øieroset M, Phan TD, Shay MA, Haggerty CC, Fujimoto M et al (2017) *Geophys Res Lett* 44(15):7598–7606. <https://doi.org/10.1002/2017GL074196>
- Øieroset M, Phan TD, Drake JF, Eastwood JP, Fuselier SA et al (2019) *Geophys Res Lett* 46(4):1937–1946. <https://doi.org/10.1029/2018GL080994>
- Pan D, Khotyaintsev YV, Graham DB, Vaivads A, Zhou X et al (2018) *Geophys Res Lett* 45(22):12116–12124. <https://doi.org/10.1029/2018GL080826>
- Petrinec SM, Burch JL, Chandler M, Farrugia CJ, Fuselier SA et al (2020) *J Geophys Res Space Phys* 125(7):e2020JA027778. <https://doi.org/10.1029/2020JA027778>
- Petrinec SM, Burch JL, Fuselier SA, Trattner KJ, Giles BL et al (2022) *J Geophys Res Space Phys* 127(6):e2021JA029669. <https://doi.org/10.1029/2021JA029669>
- Petrukovich AA, Baumjohann W, Nakamura R, Runov A, Balogh A et al (2007) *J Geophys Res Space Phys* 112(A10):A10213. <https://doi.org/10.1029/2007JA012349>
- Phan TD, Kistler LM, Klecker B, Haerendel G, Paschmann G et al (2000) *Nature* 404(6780):848–850. <https://doi.org/10.1038/35009050>
- Phan TD, Dunlop MW, Paschmann G, Klecker B, Bosqued JM et al (2004) *Ann Geophys* 22(7):2355–2367. <https://doi.org/10.5194/angeo-22-2355-2004>
- Phan TD, Paschmann G, Twitty C, Mozer FS, Gosling JT et al (2007) *Geophys Res Lett* 34(14):L14104. <https://doi.org/10.1029/2007GL030343>

- Phan TD, Love TE, Gosling JT, Paschmann G, Eastwood JP et al (2011) *Geophys Res Lett* 38:L17101. <https://doi.org/10.1029/2011GL048586>
- Phan TD, Eastwood JP, Shay MA, Drake JF, Sonnerup BUO et al (2018) *Nature* 557(7704):202–206. <https://doi.org/10.1038/s41586-018-0091-5>
- Poh G, Slavin JA, Lu S, Le G, Ozturk DS et al (2019) *J Geophys Res Space Phys* 124(9):7477–7493. <https://doi.org/10.1029/2018JA026451>
- Pu ZY, Yei M, Liu ZX (1990) *J Geophys Res* 95(A7):10559–10566. <https://doi.org/10.1029/JA095iA07p10559>
- Quijia P, Fraternali F, Stawarz JE, Vásconez CL, Perri S et al (2021) *Mon Not R Astron Soc* 503(4):4815–4827. <https://doi.org/10.1093/mnras/stab319>
- Retinò A, Sundkvist D, Vaivads A, Mozer F, André M et al (2007) *Nat Phys* 3(4):235–238. <https://doi.org/10.1038/nphys574>
- Richard L, Khotyaintsev YV, Graham DB, Sitnov MI, Le Contel O et al (2021) *J Geophys Res Space Phys* 126(8):e2021JA029152. <https://doi.org/10.1029/2021JA029152>
- Richard L, Khotyaintsev YV, Graham DB, Russell CT (2022) *Geophys Res Lett* 49(22):e2022GL101693. <https://doi.org/10.1029/2022GL101693>
- Runov A, Grandin M, Palmroth M, Batarbee M, Ganse U et al (2021) *Ann Geophys* 39(4):599–612. <https://doi.org/10.5194/angeo-39-599-2021>
- Russell CT, Elphic RC (1978) *Space Sci Rev* 22(6):681–715. <https://doi.org/10.1007/BF00212619>
- Russell CT, Qi Y (2020) *Geophys Res Lett* 47(15):1–7. <https://doi.org/10.1029/2020GL087620>
- Sauvaud J-A, Popescu D, Delcourt DC, Parks GK, Brittnacher M et al (1999) *J Geophys Res Space Phys* 104(A12):28565–28586. <https://doi.org/10.1029/1999JA900293>
- Schmid D, Volwerk M, Nakamura R, Baumjohann W, Heyn M (2011) *Ann Geophys.* <https://doi.org/10.5194/angeo-29-1537-2011>
- Scholer M (1988) *Geophys Res Lett.* <https://doi.org/10.1029/GL015i004p00291>
- Scholer M (1995) In: *Geophysical monograph series*, vol 90, pp 235–245. <https://doi.org/10.1029/GM090p0235>
- Schwartz S (1995) *Adv Space Res* 15(8–9):107–116. [https://doi.org/10.1016/0273-1177\(94\)00092-F](https://doi.org/10.1016/0273-1177(94)00092-F)
- Schwartz SJ, Kucharek H, Farrugia CJ, Trattner K, Gingell I et al (2021) *Geophys Res Lett* 48(4):e2020GL091859. <https://doi.org/10.1029/2020GL091859>
- Sergeev V, Runov A, Baumjohann W, Nakamura R, Zhang TL et al (2004) *Geophys Res Lett.* <https://doi.org/10.1029/2003GL019346>
- Sergeev VA, Sormakov DA, Apatenkov SV, Baumjohann W, Nakamura R et al (2006) *Ann Geophys* 24(7):2015–2024. <https://doi.org/10.5194/angeo-24-2015-2006>
- Sergeev VA, Apatenkov SV, Nakamura R, Plaschke F, Baumjohann W et al (2021) *J Geophys Res Space Phys* 126(2):e2020JA028694. <https://doi.org/10.1029/2020JA028694>
- Sisti M, Faganello M, Califano F, Lavraud B (2019) *Geophys Res Lett* 46(21):11597–11605. <https://doi.org/10.1029/2019GL083282>
- Sitnov MI, Buzulukova N, Swisdak M, Merkin VG, Moore TE (2013) *Geophys Res Lett* 40(1):22–27. <https://doi.org/10.1029/2012GL054701>
- Southwood DJ, Farrugia CJ, Saunders MA (1988) *Planet Space Sci* 36(5):503–508. [https://doi.org/10.1016/0032-0633\(88\)90109-2](https://doi.org/10.1016/0032-0633(88)90109-2)
- Stawarz JE, Eriksson S, Wilder FD, Ergun RE, Schwartz SJ et al (2016) *J Geophys Res Space Phys* 121(11):11021–11034. <https://doi.org/10.1002/2016JA023458>
- Stawarz JE, Eastwood JP, Genestreti KJ, Nakamura R, Ergun RE et al (2018) *Geophys Res Lett* 45(17):8783–8792. <https://doi.org/10.1029/2018GL079095>
- Sun WJ, Slavin JA, Tian AM, Bai SC, Poh GK et al (2019) *Geophys Res Lett* 46(12):6168–6177. <https://doi.org/10.1029/2019GL083301>
- Sundkvist D, Retinò A, Vaivads A, Bale SD (2007) *Phys Rev Lett* 99(2):025004. <https://doi.org/10.1103/PhysRevLett.99.025004>
- Swisdak M, Rogers BN, Drake JF, Shay MA (2003) *J Geophys Res* 108:1218. <https://doi.org/10.1029/2002JA009726>
- Swisdak M, Opher M, Drake JF, Alouani Bibi F (2010) *Astrophys J* 710(2):1769–1775. <https://doi.org/10.1088/0004-637X/710/2/1769>
- Tanaka KG, Fujimoto M, Shinohara I (2010) *Int J Geophys.* <https://doi.org/10.1155/2010/202583>
- Teh WL, Nakamura T, Nakamura R, Umeda T (2018) *J Geophys Res Space Phys* 123(10):8122–8130. <https://doi.org/10.1029/2018JA025775>
- Terasawa T, Fujimoto M, Mukai T, Shinohara I, Saito Y et al (1997) *Geophys Res Lett* 24(8):935–938. <https://doi.org/10.1029/96GL04018>
- Torbert RB, Burch JL, Giles BL, Gershman D, Pollock CJ et al (2016) *Geophys Res Lett* 43(12):5918–5925. <https://doi.org/10.1002/2016GL069553>

- Torbert RB, Burch JL, Phan TD, Hesse M, Argall MR et al (2018) *Science* 362(6421):1391–1395. <https://doi.org/10.1126/science.aat2998>
- Trattner KJ, Mulcock JS, Petrinec SM, Fuselier SA (2007) *J Geophys Res Space Phys* 112(A8):A08210. <https://doi.org/10.1029/2007JA012270>
- Trattner KJ, Fuselier SA, Petrinec SM, Burch JL, Ergun R et al (2021a) *J Geophys Res Space Phys* 126(4):e2020JA028926. <https://doi.org/10.1029/2020JA028926>
- Trattner KJ, Petrinec SM, Fuselier SA (2021b) *Space Sci Rev* 217(3):41. <https://doi.org/10.1007/s11214-021-00817-8>
- Varsani A, Nakamura R, Sergeev VA, Baumjohann W, Owen CJ et al (2017) *J Geophys Res Space Phys* 122(11):10891–10909. <https://doi.org/10.1002/2017JA024547>
- Vernisse Y, Lavraud B, Eriksson S, Gershman DJ, Dorelli J et al (2016) *J Geophys Res Space Phys* 121(10):9926–9939. <https://doi.org/10.1002/2016JA023051>
- Vernisse Y, Lavraud B, Faganello M, Fadanelli S, Sisti M et al (2020) *J Geophys Res Space Phys* 125(5):e2019JA027333. <https://doi.org/10.1029/2019JA027333>
- Wang R, Lu Q, Nakamura R, Baumjohann W, Russell CT et al (2017) *J Geophys Res Space Phys* 122(10):10436–10447. <https://doi.org/10.1002/2017JA024482>
- Wang R, Lu Q, Nakamura R, Baumjohann W, Huang C et al (2018) *Geophys Res Lett* 45(10):4542–4549. <https://doi.org/10.1002/2017GL076330>
- Wang S, Chen L, Bessho N, Hesse M, Wilson LB et al (2019) *Geophys Res Lett* 46(2):562–570. <https://doi.org/10.1029/2018GL080944>
- Webster JM, Burch JL, Reiff PH, Daou AG, Genestreti KJ et al (2018) *J Geophys Res Space Phys* 123(6):4858–4878. <https://doi.org/10.1029/2018JA025245>
- Wei YY, Huang SY, Rong ZJ, Yuan ZG, Jiang K et al (2019) *Astrophys J* 874(2):L18. <https://doi.org/10.3847/2041-8213/ab0f28>
- Wellenzohn S, Nakamura R, Nakamura TKM, Varsani A, Sergeev VA et al (2021) *J Geophys Res Space Phys* 126(1):e2020JA028917. <https://doi.org/10.1029/2020JA028917>
- Wing S, Johnson JR, Newell PT, Meng C-I (2005) *J Geophys Res Space Phys* 110(A8):A08205. <https://doi.org/10.1029/2005JA011086>
- Xu Y, Fu H, Cao J, Liu C, Norgren C et al (2021) *Geophys Res Lett* 48(6):e2020GL092232. <https://doi.org/10.1029/2020GL092232>
- Yordanova E, Vörös Z, Raptis S, Karlsson T (2020) *Front Astron Space Sci* 7:1–11. <https://doi.org/10.3389/fspas.2020.00002>
- Zenitani S, Hesse M, Klimas A, Kuznetsova M (2011) *Phys Rev Lett* 106:195003. <https://doi.org/10.1103/PhysRevLett.106.195003>
- Zhong ZH, Zhou M, Deng XH, Song LJ, Graham DB et al (2021) *Geophys Res Lett* 48(1):2020GL090946. <https://doi.org/10.1029/2020GL090946>
- Zhou M, Berchem J, Walker RJ, El-Alaoui M, Deng X et al (2017) *Phys Rev Lett*. <https://doi.org/10.1103/PhysRevLett.119.055101>

Publisher's Note Springer Nature remains neutral with regard to jurisdictional claims in published maps and institutional affiliations.

Authors and Affiliations

K.-J. Hwang¹  · R. Nakamura² · J.P. Eastwood³ · S.A. Fuselier¹ · H. Hasegawa⁴ · T. Nakamura^{5,6} · B. Lavraud⁷ · K. Dokgo¹ · D.L. Turner⁸ · R.E. Ergun⁹ · P.H. Reiff¹⁰

✉ K.-J. Hwang
joo.hwang@swri.org

✉ R. Nakamura
rumi.nakamura@aew.ac.at

¹ Southwest Research Institute, San Antonio, TX, USA

² Space Research Institute, Austrian Academy of Sciences ÖAW, Graz, Austria

³ Imperial College, London, UK

- 4 Institute of Space and Astronautical Science, Japan Aerospace Exploration Agency, Sagami-hara, Japan
- 5 Austrian Academy of Sciences ÖAW, Space Research Institute, Vienna, Austria
- 6 Krimgen LLC, 732-0828, Hiroshima, Japan
- 7 Institut de Recherche en Astrophysique et Planétologie, CNRS, UPS, CNES, Université de Toulouse, Toulouse, France
- 8 The Johns Hopkins Applied Physics Laboratory, Laurel, MD, USA
- 9 Laboratory for Atmospheric and Space Physics, University of Colorado at Boulder, Boulder, CO, USA
- 10 Rice University, Houston, TX, USA